www.pnas.org

Supplementary Information for

Supporting Information for: Unifying deterministic and stochastic ecological dynamics via a landscape-flux approach

Li Xu, Denis Patterson, Ann Carla Staver, Simon Asher Levin* and Jin Wang*

*** E-mail: slevin@princeton.edu, jin.wang.1@stonybrook.edu**

This PDF file includes:

Supplementary text
Figs. S1 to S44 (not allowed for Brief Reports)
Table S1 (not allowed for Brief Reports)
SI References

Supporting Information Text

Table S1 below summarizes the mathematical definitions and notation used throughout the paper.

Table S1. Mathematical Variables

Symbol	Interpretation
$\mathbf{x}$	system state
$\mathbf{F}(\mathbf{x})$	driving force
D	scale factor representing the magnitude of the fluctuations
$\mathbf{G}$	diffusion matrix
$P(\mathbf{x}, t)$	probability of system state $\mathbf{x}$ at time t
$\mathbf{J}(\mathbf{x}, t)$	probability flux
J_{ss}	probability flux of steady state
$U(\mathbf{x})$	population potential landscape
ϕ_0	intrinsic potential landscape
$\mathbf{V}$	intrinsic flux velocity
$L(\mathbf{x})$	Lagrangian
$\mathcal{F}$	intrinsic free energy
$\mathcal{Z}$	partition function

Remark

The Fokker-Planck equation for the evolution of the probability density and the corresponding Langevin equation for the evolution of the stochastic trajectories are usually mathematically equivalent in terms of the statistics(1–3). However, in practice, the diffusion equation cannot always be used to deal with dimensions more than four due to memory issues, while the Langevin trajectory method can more easily explore higher dimensions. This is due to the fact that stochastic Langevin method only samples the higher probability states, thus saving computational times when exploring the state space. We use both of these methods according to their convenience and computational cost. For example, the steady state probability density result can be readily obtained from the Fokker-Planck equation in low dimensions, while the distribution of kinetic times and the variances of the frequencies for the Savanna state (resp. Forest state) can be directly calculated from the Langevin trajectories.

1. Ecological behavior as a function of the sapling birth rate β. The dominant population path is the path of transition from one stable state to the other with the largest probability and can thus be used to understand *Savanna* to *Forest* or *Forest* to *Savanna* transitions in the SL model. The dominant population path probability can in turn be quantified by the population action $A_{po}(\mathbf{x})$, as shown in Figure S1A. A_{poFS} denotes the action of the dominant population path from *Forest* to *Savanna* and A_{poSF} denotes the action of the dominant population path from *Savanna* to *Forest*. Higher action denotes lower dominant population path probability since the dominant population path probability is proportional to $\exp[-A(\mathbf{x})]$. As expected, we observe that A_{poFS} increases and A_{poSF} decreases with increasing β. Figure S1D shows the logarithm of the dominant population path probability from *Forest* to *Savanna* divided by that of the dominant population path from *Savanna* to *Forest* decreases as β becomes bigger. Thus *Savanna* becomes less stable while *Forest* becomes more stable as β increase. Thus, it becomes harder to switch from *Forest* to *Savanna*, while it becomes easier to switch from *Savanna* to *Forest*. We also show that the action of the dominant population path versus μ, θ_1 in Figure S1.

Figure S2 shows the intrinsic potential landscape ϕ_0 for increasing β overlaid with the intrinsic flux velocity (purple arrows) and the negative gradient of the intrinsic potential landscape $-\nabla\phi_0$ (white arrows), as well as the intrinsic paths (thick red/white lines). Once more, as expected, we observe a shift from *Savanna* to *Forest* dominance as β increases. The dominant intrinsic path from *Savanna* to *Forest*, and the dominant intrinsic path from *Forest* to *Savanna* are distinct. The irreversibility of the dominant intrinsic paths is due to the presence of the nonequilibrium rotational flux and the two intrinsic dominant intrinsic paths both pass through the saddle point (the black dot) which shows that the dominant intrinsic paths must pass through the saddle point under zero fluctuations. In the zero fluctuation limit, the force can be decomposed into a gradient term and a curl term: $\mathbf{F} = -\mathbf{G} \cdot \nabla\phi_0 + \mathbf{V}$. Hence the two components of the driving force for the ecological system are the negative gradient of the intrinsic potential landscape $-\nabla\phi_0$ (white arrows) and the intrinsic steady-state flux velocity $\mathbf{V}$ (purple arrows). The intrinsic flux (purple arrows) and the negative gradient of the intrinsic potential landscape $(-\nabla\phi_0)$(white arrows) are perpendicular to each other because $\mathbf{V} \cdot \nabla\phi_0 = 0$. As β increases, the intrinsic potential landscape varies from *Grassland* to *Savanna*, and then *Forest* emerges and becomes more stable than *Savanna* until *Savanna* eventually vanishes.

The intrinsic path weights are the probabilities of each route for state switching in the zero fluctuation limit and thus quantify the likelihood of different transition routes. Similarly, the dominant intrinsic path weight is the probability of the dominant switching path and thus quantifies the dominant transition routes. The dominant intrinsic path probability can in turn be quantified by the intrinsic action $A_{in}(\mathbf{x})$(shown in Figure S3A). A_{inFS} is the intrinsic action of the dominant intrinsic path from *Forest* to *Savanna* and A_{inSF} is the intrinsic action of the dominant intrinsic path from *Savanna* to *Forest*. Figure S3D shows that the logarithm of the dominant intrinsic path probability from *Forest* to *Savanna* divided by that of the dominant intrinsic path from *Savanna* to *Forest* decreases as β increases. Thus the dominant intrinsic path probability from

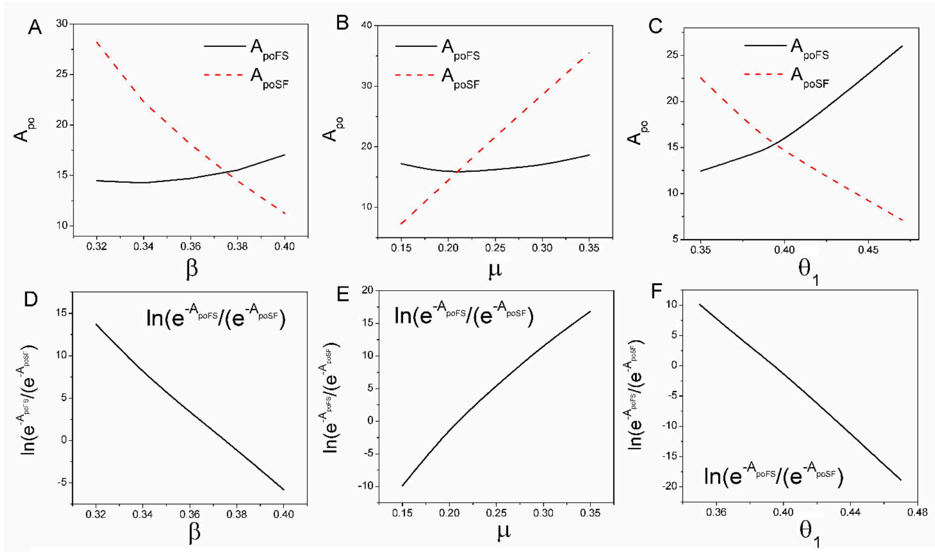

Fig. S1. A: The population action A_{poFS} of the probability of the dominant population path from $Forest$ to $Savanna$ and the population action A_{poSF} of the probability of the dominant population path from $Savanna$ to $Forest$ versus β. D: The probability of the dominant population path from $Forest$ to $Savanna$ divided by that of the dominant population path from $Savanna$ to $Forest$ versus β. B: The population action A_{poFS} and A_{poSF} versus μ. E: The probability of the dominant population path from $Forest$ to $Savanna$ divided by that of the dominant population path from $Savanna$ to $Forest$ versus μ. C: The population action A_{poFS} and A_{poSF} versus θ_1. F: The probability of the dominant population path from $Forest$ to $Savanna$ divided by that of the dominant population path from $Savanna$ to $Forest$ versus θ_1.

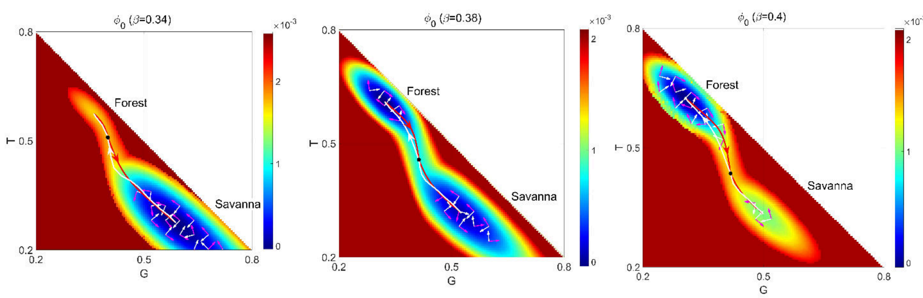

Fig. S2. The non-equilibrium intrinsic potential landscape ϕ_0 for increasing β. The white lines are the dominant intrinsic paths from the $Savanna$ to $Forest$, while red lines are the dominant intrinsic paths from the $Forest$ to $Savanna$. Purple arrows are the projection of the flux velocity and white arrows are the projection of the negative gradient of the intrinsic potential landscape $-\nabla\phi_0$.

Forest to *Savanna* decreases (or the dominant intrinsic path from *Savanna* to *Forest* increases) as β becomes larger. We also show that the intrinsic action of the dominant intrinsic path for μ, θ_1 in Figure S3.

Figure S4 shows the population barrier heights versus parameter A: β, B:μ, C: θ_1, D:ν, E:ω_0, F:ω_1. Figure S5 shows the intrinsic barrier heights versus parameter A: β, B:μ, C: θ_1, D:ν, E:ω_0, F:ω_1. Figure S6 shows the logarithm of MFPT versus A: β, B:μ, C: θ_1. The logarithm of MFPT versus barrier heights for D: β, E:μ, F: θ_1.

2. Ecological behavior as a function of the Savanna Sapling Mortality Rate μ.

2.1. Landscape, flux and dominant paths between different states versus Savanna Sapling Mortality Rate μ.

2.1.a. Non-equilibrium population-potential landscape and the flux in finite fluctuation. μ represents savanna sapling mortality rate. Figure S7A shows the deterministic phase diagram mapping the fraction of Grass cover versus μ. When the savanna sapling mortality rate is small the only one stable state is *Forest*, but as μ is increased, *Forest* loses stability to *Savanna*. For μ between about 0.14 and 0.37, bistability emerges. Beyond 0.37, the dynamics are dominated by *Savanna*. For μ larger than 0.37 but less than 0.65, the *Grassland* $[1,0]$ state is always stable on the G-axis and unstable on the T-axis; For μ beyond 0.65, the *Grassland* state becomes stable. The corresponding stochastic phase diagram with respect to μ ($D = 0.0001$), in which stable states correspond to local minima of the population-potential landscape, is shown in Figure 9B in the main text. Remarkably, the *Grassland* states becomes quasi-stable for much lower values of μ in the stochastic phase diagram, indicating a fragility of the *Forest* ecological system which is purely induced by the stochastic fluctuations.

We now describe the concept and computation of the "stochastic phase diagram". When a deterministic nonlinear system has multiple steady states, stochastic forcing can lead to the system to switch between the various attractors. The steady-state probability density of the stochastic system can show multiple peaks and the topological shape of the steady-state probability

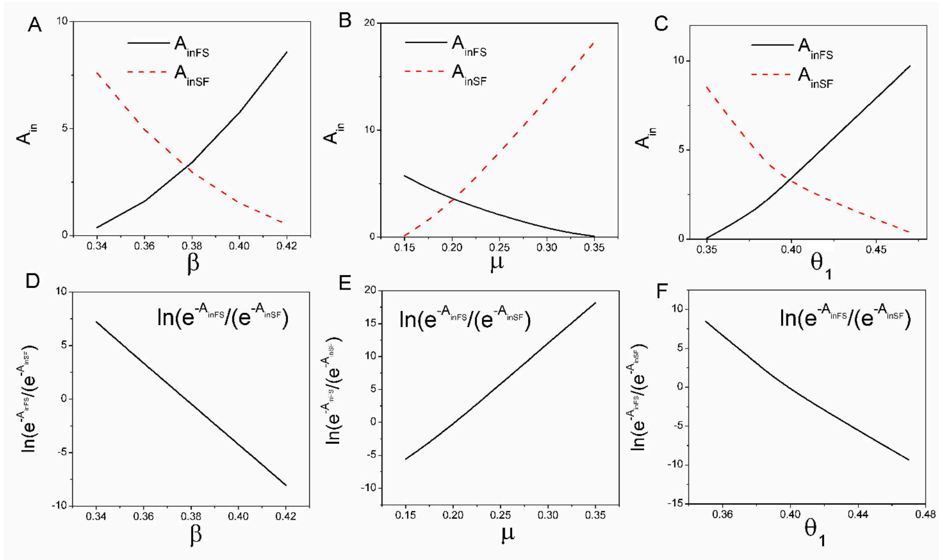

Fig. S3. A: The intrinsic action A_{inFS} of the probability of the intrinsic dominant intrinsic path from *Forest* state to *Savanna* state and the intrinsic action A_{inSF} of the probability of the intrinsic dominant intrinsic path from *Savanna* state to *Forest* state versus β. D:The probability of the dominant intrinsic path from *Forest* state to *Savanna* state divided that of the dominant intrinsic path from *Savanna* state to *Forest* state versus β. B: The intrinsic action A_{inFS} and A_{inSF} versus μ. E:The probability of the dominant intrinsic path from *Forest* state to *Savanna* state divided that of the dominant intrinsic path from *Savanna* state to *Forest* state versus μ. C: The intrinsic action A_{inFS} and A_{inSF} versus θ_1. F:The probability of the dominant intrinsic path from *Forest* state to *Savanna* state divided that of the dominant intrinsic path from *Savanna* state to *Forest* state versus θ_1.

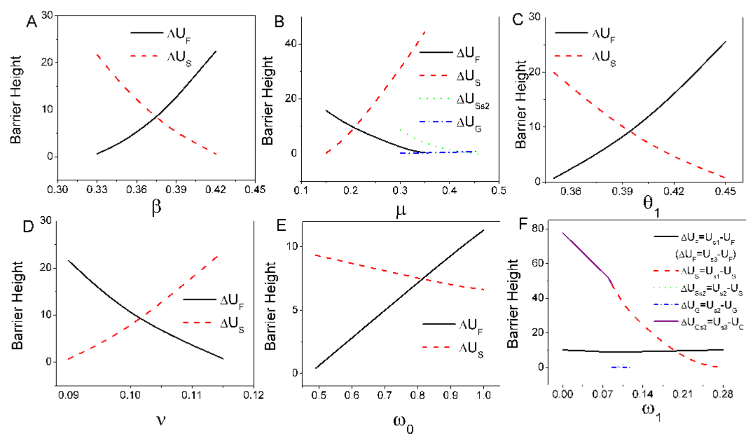

Fig. S4. The population barrier heights versus parameter A: β, B:μ, C: θ_1, D:ν, E:ω_0, F:ω_1

density can change as parameters vary. This may lead to the emergence of the so-called stochastic P bifurcation (4). Since our model has a two dimensional state space the analytical expression for the phase diagram is often not available. Nevertheless, the stochastic phase diagram can be obtained numerically through the behavior of the population barrier height ΔU_G under the finite fluctuations (we chose $D = 0.0001$), where ΔU_G represents the barrier height from *Grassland* state basin to the *Savanna* state basin. We find that the population barrier height ΔU_G approaches zero as μ decreases to nearly $\mu = 0.3$. This indicates that the *Grassland* state vanishes as μ decreases to nearly $\mu = 0.3$ under the finite fluctuations of $D = 0.0001$ shown in Figure 9 in the main text.

Figure S8 shows the population-potential landscapes for increasing μ and Figure S9 shows the fluxes on the population-potential landscapes (white arrows). Only stable state, *Forest*, is present when μ is sufficiently small. As sapling mortality rate μ increases, the ecological transitions from *Forest* dominant to *Savanna* dominant, as shown in Figure S7A. As mortality further increases, the *Forest* state is no longer stable and the remaining two stable states coexist: the coexistence of the *Savanna* and the *Grassland* states. Eventually, at very high mortality rates, trees can no longer survive and the ecological system is left with a unique stable attractor: *Grassland* ([1, 0]). In Figure S9, we can see that both the negative gradient of the population-potential landscapes and the non-zero flux are the driving forces for the dynamics of the forest-savanna ecological system. When the system has both the *Savanna* and the *Forest* stable states, the fluxes originating from the vegetative growth factors tend to enhance communications between the two stable states.

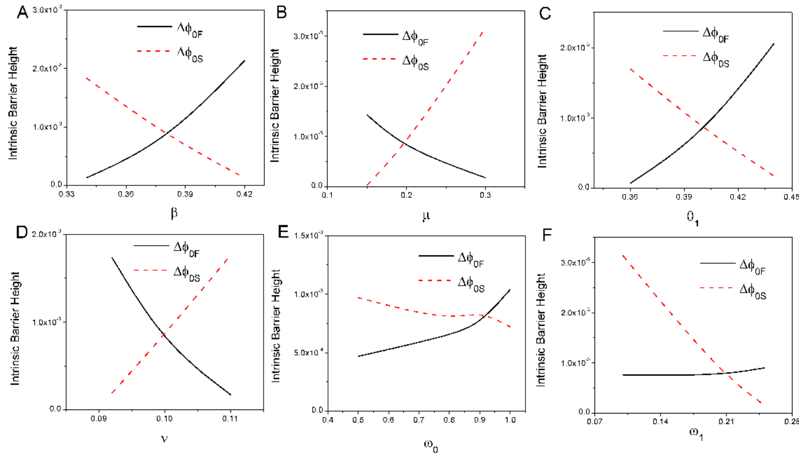

Fig. S5. The intrinsic barrier heights versus parameter A: β, B:μ, C: θ_1, D:ν, E:ω_0, F:ω_1.

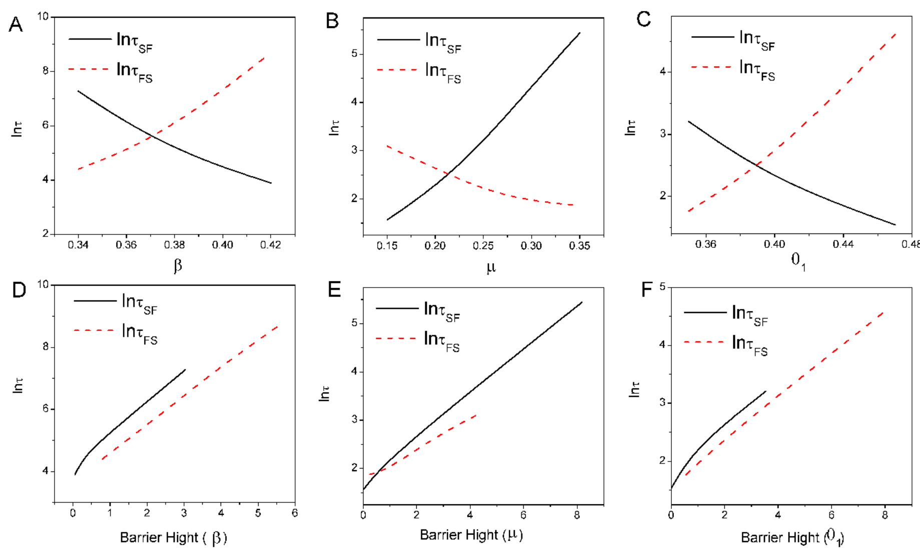

Fig. S6. The logarithm of MFPT versus A: β, B:μ, C: θ_1. The logarithm of MFPT versus barrier heights for D: β, E:μ, F: θ_1.

Figure S9 also shows the dominant population paths on the population landscape U for different values of μ. The dominant population path probability can be quantified by the population action $A_{po}(\mathbf{x})$ shown in Figure S1B. Figure S1E shows the logarithm of the dominant population path probability from the *Forest* state to the *Savanna* state divided by that of the dominant population path from the *Savanna* state to the *Forest* state.

2.1.c. Intrinsic potential landscape and flux velocity in the zero-fluctuation limit. Figure S10 shows the intrinsic potential landscape ϕ_0 versus μ. The intrinsic potential landscape changes from *Forest* dominant to *Savanna* and *Forest* coexistence, and then to *Savanna* dominant as μ increases.

Figure S11 shows the two-dimensional non-equilibrium intrinsic potential landscape ϕ_0 under the zero fluctuation limit for increasing μ. We concentrate on the parameter range of the coexistence of the two stable states in these two-dimensional landscape figures since the complete phase changes of the intrinsic potential landscapes in the whole parameter range have already been shown in the three-dimensional figure.

Figure S11 also shows the dominant intrinsic paths on the intrinsic potential landscape ϕ_0 with different μ. The red lines represent the dominant intrinsic paths from the *Forest* state to the *Savanna* state. The white lines represent the dominant intrinsic paths from the *Savanna* state to the *Forest* state. The purple arrows represent the steady-state probability intrinsic fluxes which guide the dominant intrinsic paths apart from the steepest descent path from the intrinsic potential landscape. Therefore, the dominant intrinsic path from the *Savanna* state to the *Forest* state and the dominant intrinsic path from the *Forest* state to the *Savanna* state are distinct; this is referred to as irreversibility of the dominant intrinsic paths and is due to the presence of the nonequilibrium rotational intrinsic flux. The two dominant intrinsic paths both pass through the saddle

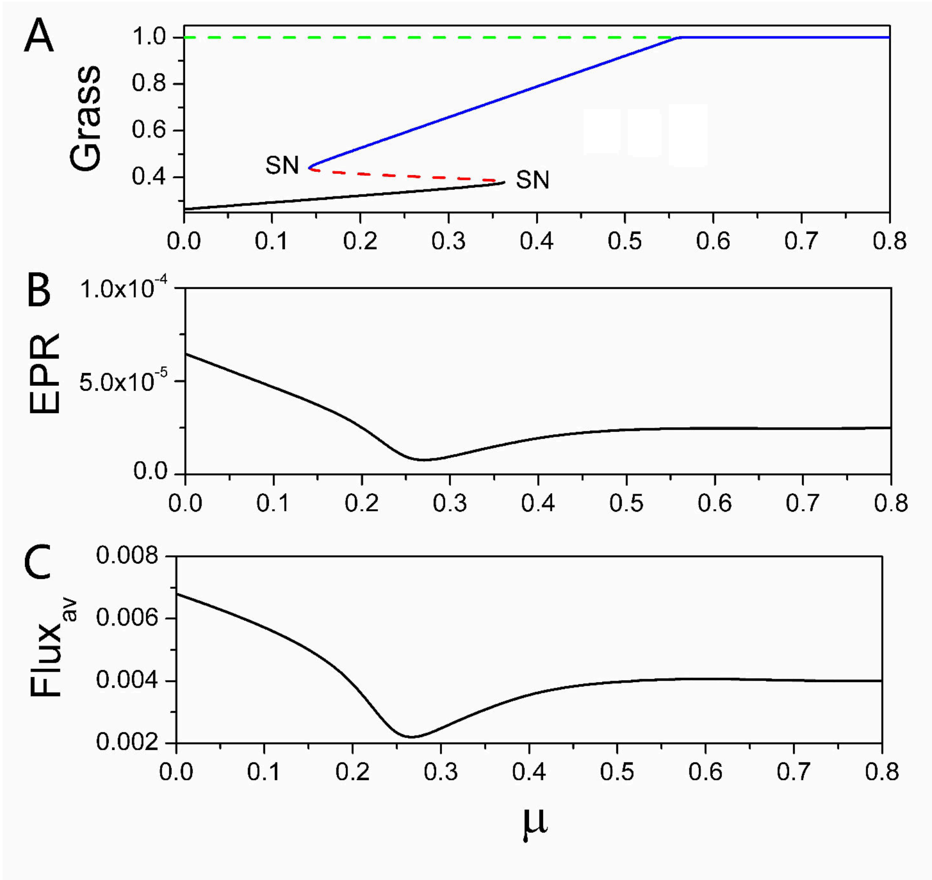

Fig. S7. A: The phase diagram versus parameter μ. B: The population entropy production rate versus parameter μ. C: The population average flux versus parameter μ.

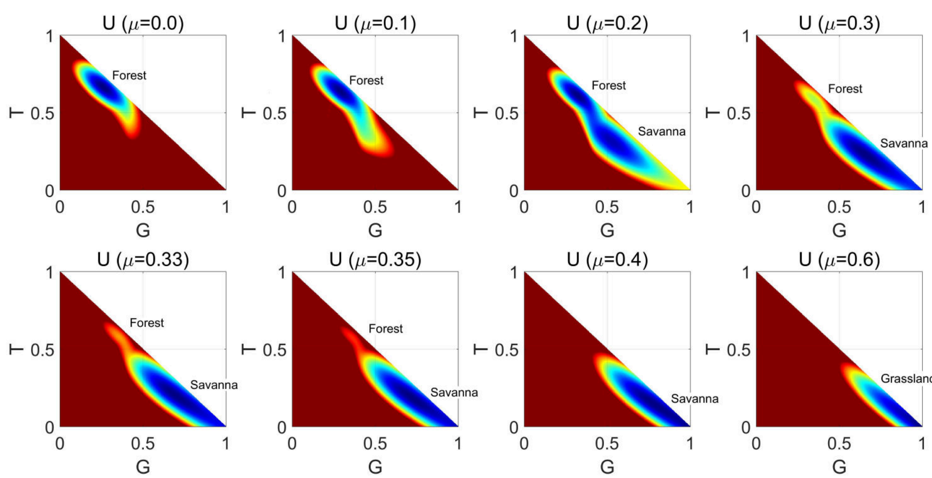

Fig. S8. The two-dimensional population-potential landscapes versus parameter μ.

point (the black dot) on the figures.

The dominant intrinsic path probability can be quantified by the intrinsic action $A_{in}(\mathbf{x})$, which is shown in Figure S3B. Figure S3E shows the logarithm of the dominant intrinsic path probability from the *Forest* state to the *Savanna* state divided by that of the dominant intrinsic path from the *Savanna* state to the *Forest* state increases as μ becomes larger.

2.2.Barrier height and kinetic rates of switching. Figures S4B and S5B show the barrier heights of the population-potential landscape and the intrinsic barrier heights of the intrinsic potential landscape versus μ. Here, ΔU_G is the population barrier height from the *Grassland* state to the saddle point s_2 between the *Grassland* state and the *Savanna* state. ΔU_{Ss_2} is the population barrier height from the *Savanna* state to the saddle point s_2. We show the logarithm of MFPT versus μ in Figure S6B and we

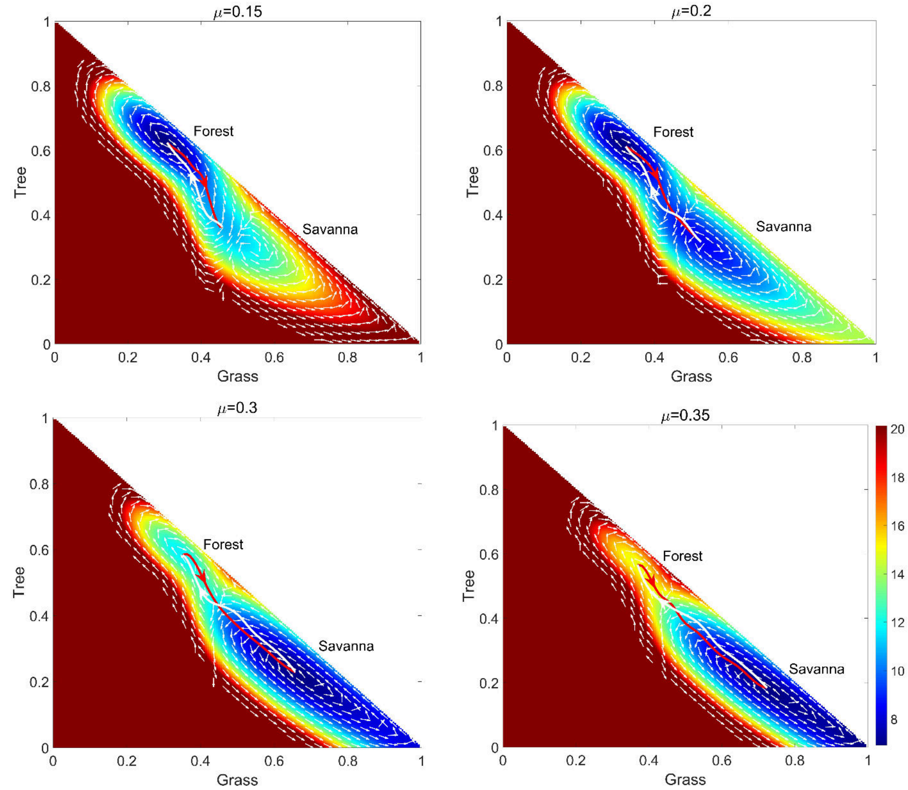

Fig. S9. The dominant population paths and fluxes on the population-potential landscape U with different μ, at $\beta = 0.38, \nu = 0.1, \omega_0 = 0.9, \omega_1 = 0.2, \theta_1 = 0.4, s_1 = 0.01$, $D = 0.0005$. The white lines represent the dominant population paths from the $Savanna$ state to $Forest$ state. The red lines represent the dominant population paths from the $Forest$ state to $Savanna$ state. The white arrows represent the steady-state probability fluxes.

observe that the population-potential landscape topography (quantified by the barrier height) and the logarithm of MFPT have positive correlation (Figure S6E). Thus, the barrier heights ΔU_F and ΔU_S, and the corresponding MFPTs $ln\tau_{FS}$ and $ln\tau_{SF}$ are correlated as $\tau \sim exp(\Delta U)$.

2.3. Bifurcation diagrams, nonequilibrium flux and nonequilibrium thermodynamic cost.

2.3.a. Finite fluctuations. Figure S7B shows the population entropy production rate versus μ and Figure S7C shows the population average flux versus μ. Both population EPR and population $Flux_{av}$ decrease initially and then increase as μ increases, and both undergo significant changes in their slopes in the bifurcation zone between the two transitions shown in Figure S7B and Figure S7C. This shows that the significant changes of average flux and entropy production may be a signal of bifurcation. Therefore we can use the population average flux and population entropy production rate to quantify the global stability and bifurcations of the ecological system. We found that the *Forest* state has more EPR and $Flux_{av}$, implying that the trees need more vegetative growth factors, and require more nutrition and energy than grass from the environment. On the other hand, the *Savanna* state needs less vegetative growth factors, and requires less nutrition and energy than trees from the environment.

The savanna-forest model we studied is a phenomenological model. The entropy production and dissipation cost in this study are both obtained based on the model given. The entropy production and dissipation cost are thus calculated according to the driving force and the associated dynamics of this model. They represent the global thermodynamic cost for the whole system. It turns out that this global cost is directly related to the flux (approximately integral of the square of the flux modulated by the diffusion coefficient over state space). This is the link between the nonequilibrium thermodynamics and the nonequilibrium dynamics.

If one wants to know the specifics and details of the entropy and energy partition among trees/grass, further explorations are needed with a more detailed microscopic model by identifying the source of the cost in growing trees explicitly. Extending our analysis in this direction would be an interesting topic for future study. However, a more detailed microscopic model should lead to the same conclusion as the phenomenological model we used here, at least in terms of the global dynamics and thermodynamics at the macroscopic level.

2.3.b. The zero fluctuation limit. Figure S12A shows two phase transition points for this set of parameters and Figure S12B shows the intrinsic entropy production rate versus μ. Figure S12C shows the intrinsic average flux versus μ, while Figure S12C shows that the intrinsic $Flux_{av}$ and entropy production rate have similar shapes. Both the intrinsic averaged flux and intrinsic entropy production rate have significant changes along with the bifurcation shown in Figure S12A. The slope of the non-equilibrium

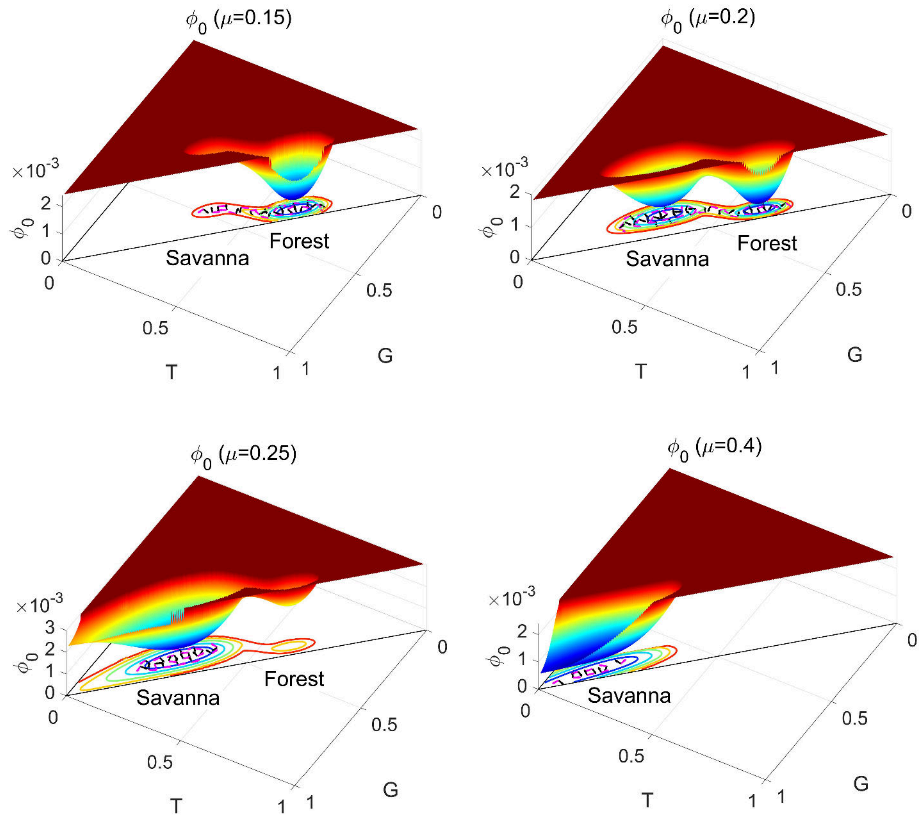

Fig. S10. The three-dimensional intrinsic potential landscape ϕ_0 for increasing μ. The projection of the flux velocity (purple arrows)and the gradient of the intrinsic potential landscape $-\nabla\phi_0$ (black arrows)on the intrinsic potential landscape ϕ_0 for increasing μ.

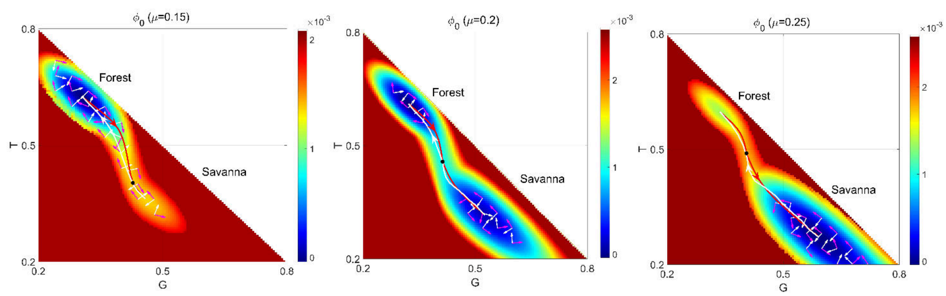

Fig. S11. The projection of the flux velocity (purple arrows)and the gradient of the intrinsic potential landscape $-\nabla\phi_0$ (white arrows)on the intrinsic potential landscape ϕ_0 for increasing μ. The dominant intrinsic paths on the intrinsic potential landscape ϕ_0 with different μ. The white lines represent the dominant intrinsic paths from the $Savanna$ state to $Forest$ state. The red lines represent the dominant intrinsic paths from the $Forest$ state to $Savanna$ state.

intrinsic free energy changes significantly between the two saddle-node bifurcations, although the non-equilibrium intrinsic free energy is continuous. Figure S12B, Figure S12C and Figure S12D show that significant slope changes in intrinsic entropy production rate, intrinsic average flux and intrinsic free energy (analogous to the equilibrium case) may provide signals of bifurcation. We can see that the non-equilibrium intrinsic free energy may also be useful to quantify the global phases of the system and the bifurcations. Therefore, we may use this non-equilibrium intrinsic free energy function as well as the intrinsic average flux and intrinsic entropy production rate to explore the global stability and bifurcations of the non-equilibrium ecological dynamics.

3. Ecological behavior as a function of the grass cover basic value θ_1.

3.1.Landscape, flux and dominant paths.

3.1.a. Population-potential landscape and flux with finite fluctuation. θ_1 represents grass cover basic value, i.e. the threshold onset value for the fire rate sigmoid ω. Figure S13A shows the phase diagram versus θ_1, Figure S13B shows the population entropy production rate versus θ_1, and Figure S13C shows the average flux versus θ_1. Figure S14 shows the two-dimensional

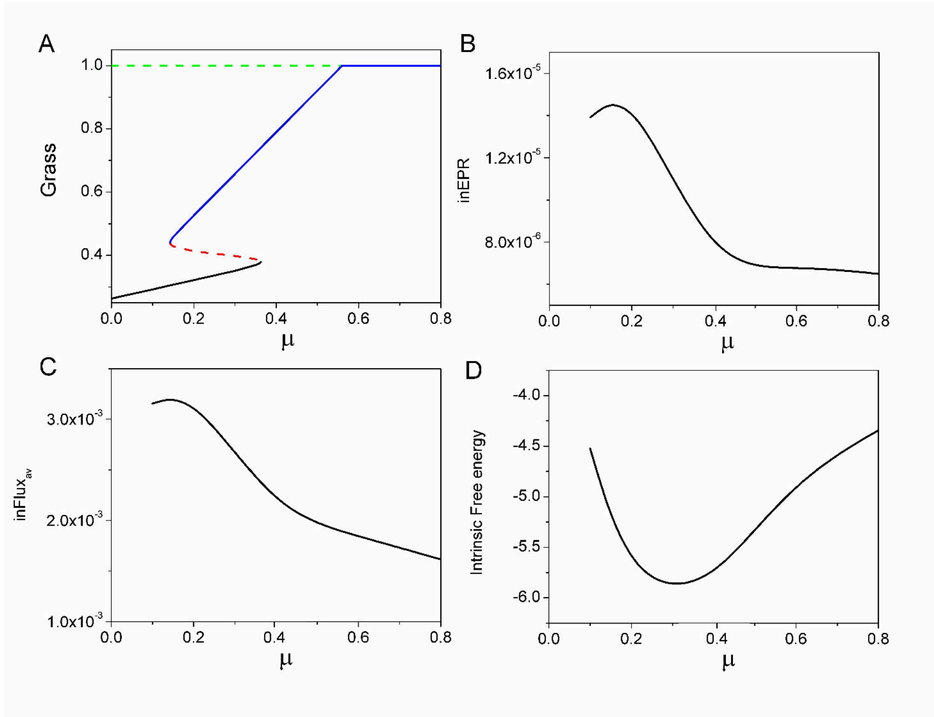

Fig. S12. A: The phase diagram versus μ. B: The intrinsic entropy production rate versus μ. C: The intrinsic average flux versus μ. D: Intrinsic free energy versus μ.

population-potential landscapes under finite fluctuations varying with the increase of θ_1. Figure S15 shows the steady-state probability fluxes under the increase of θ_1, which are shown as the white arrows. Figure S15 also shows the dominant population paths on the population landscape U for different values of θ_1 with the population action $A_{po}(\mathbf{x})$ shown in Figure S1C.

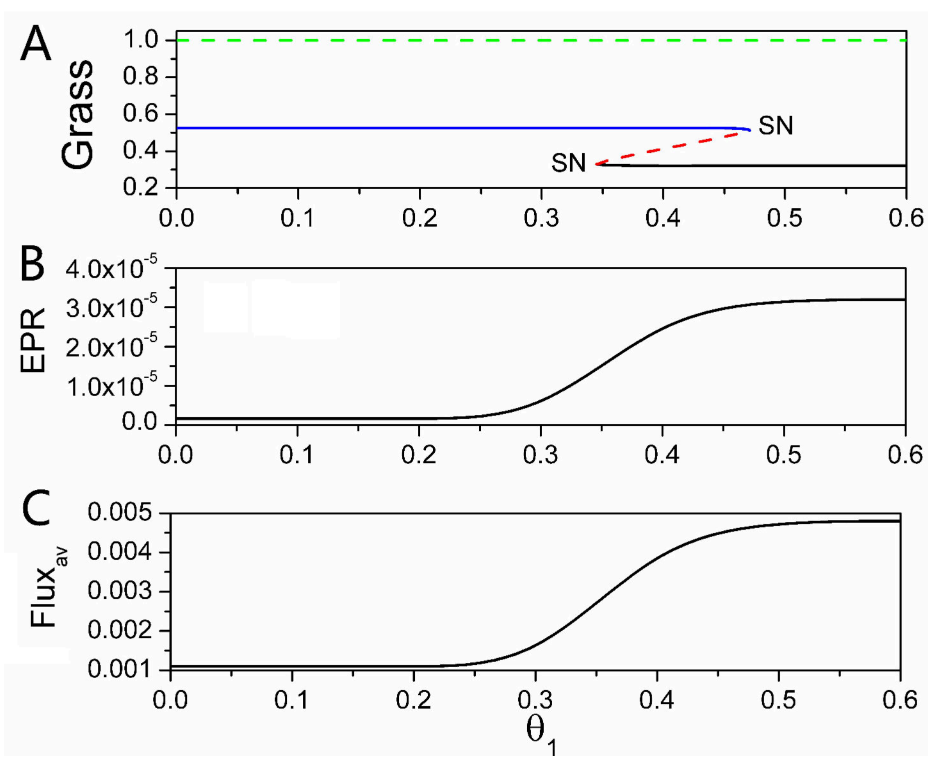

Fig. S13. A: The phase diagram versus θ_1. B: The population entropy production rate versus θ_1. C: The population average flux versus θ_1.

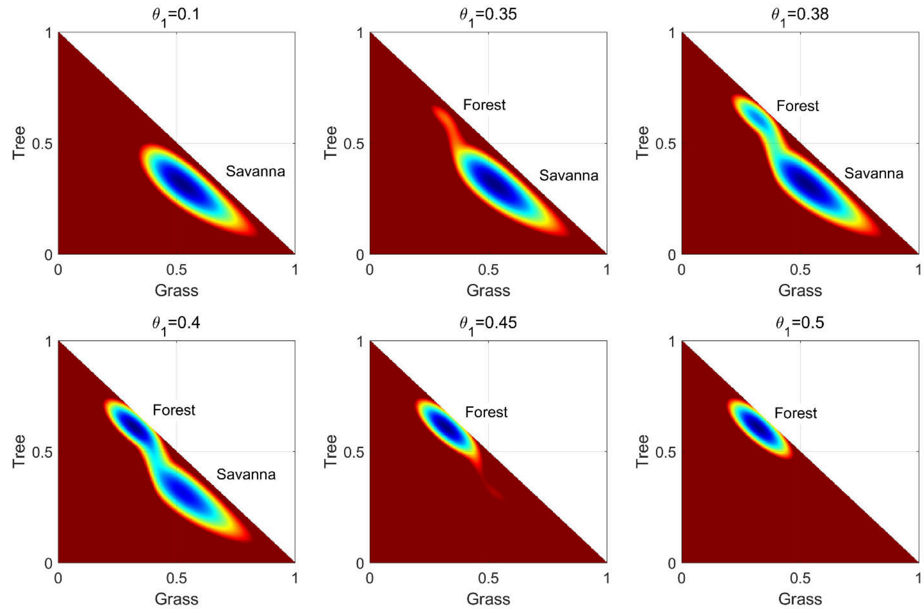

Fig. S14. The two-dimensional population-potential landscapes versus θ_1.

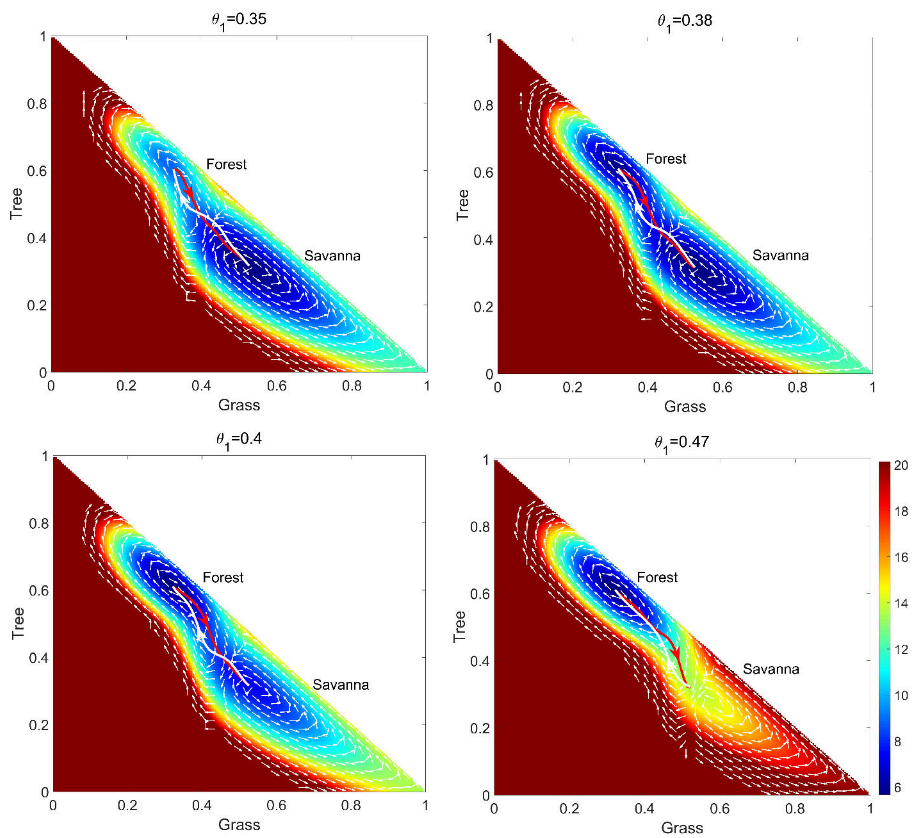

Fig. S15. The dominant population paths and fluxes on the population-potential landscape U with different θ_1, at $\beta = 0.38, \nu = 0.1, \omega_0 = 0.9, \omega_1 = 0.2, \mu = 0.2, s_1 = 0.01$, $D = 0.0005$. The white lines represent the dominant population paths from the $Savanna$ state to $Forest$ state. The red lines represent the dominant population paths from the $Forest$ state to $Savanna$ state. The white arrows represent the steady-state probability fluxes.

3.1.b. Non-equilibrium intrinsic potential landscape and flux velocity in the zero-fluctuation limit. Figure S16 shows the intrinsic potential landscape ϕ_0 and Figure S17 shows the non-equilibrium intrinsic potential landscape ϕ_0 in the zero fluctuation limit, both for increasing values of θ_1. Figure S17 also shows the dominant intrinsic paths on the intrinsic potential landscape ϕ_0 for different values of θ_1. The red lines are the dominant intrinsic paths from the *Forest* state to *Savanna* state, while the white lines are the dominant intrinsic paths from the *Savanna* state to *Forest* state. Finally, the purple arrows represent the steady-state probability intrinsic fluxes which guide the dominant intrinsic paths. The intrinsic action $A_{in}(\mathbf{x})$ is shown in Figure S3C and Figure S3F shows the logarithm of the dominant intrinsic path probability from the *Forest* state to the *Savanna* state divided by that of the dominant intrinsic path from the *Savanna* state to the *Forest* state.

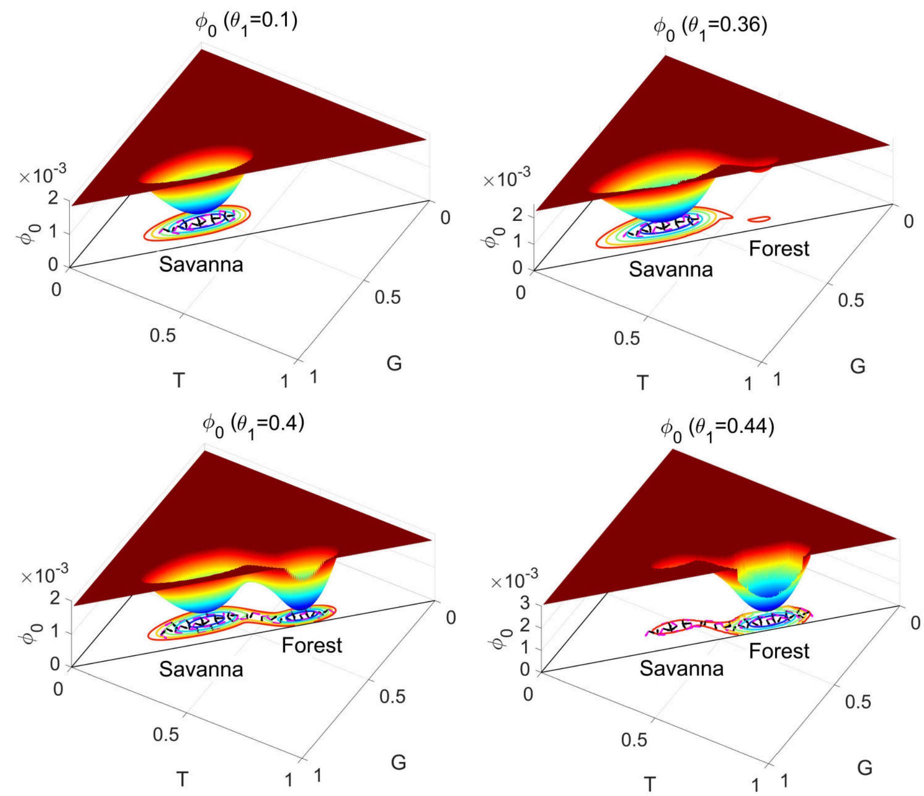

Fig. S16. The three-dimensional intrinsic potential landscape ϕ_0 for increasing θ_1. The projection of the flux velocity (purple arrows)and the gradient of the intrinsic potential landscape $-\nabla\phi_0$ (black arrows)on the intrinsic potential landscape ϕ_0.

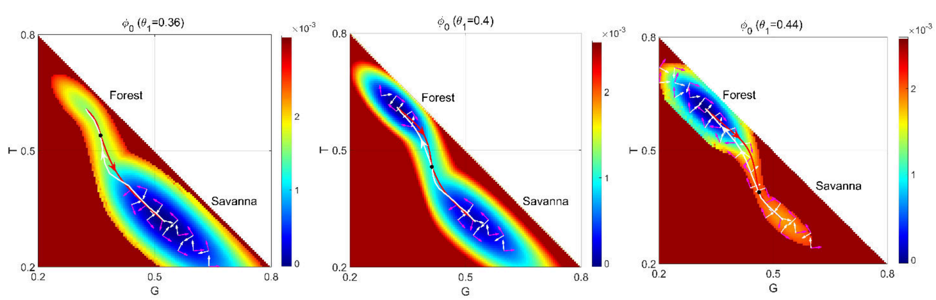

Fig. S17. The projection of the flux velocity (purple arrows)and the gradient of the intrinsic potential landscape $-\nabla\phi_0$ (white arrows)on the intrinsic potential landscape ϕ_0 for increasing θ_1. The dominant intrinsic paths on the intrinsic potential landscape ϕ_0 with different θ_1. The white lines represent the dominant intrinsic paths from the $Savanna$ state to $Forest$ state. The red lines represent the dominant intrinsic paths from the $Forest$ state to $Savanna$ state.

3.2.Barrier height and kinetic rates of switching. Figure S4C and Figure S5C show the barrier heights of the population-potential landscape and the intrinsic barrier heights of the intrinsic potential landscape versus θ_1 respectively. The logarithm of MFPT versus θ_1 are shown in Figure S6C and we see that the population-potential landscape topography, quantified by the barrier height, and the corresponding logarithm of MFPT have positive correlation, as shown in Figure S6F. Thus, the barrier height ΔU_F, ΔU_S and the corresponding MFPT $ln\tau_{FS}$ and $ln\tau_{SF}$ have the correlations as $\tau \sim exp(\Delta U)$.

3.3. Bifurcation diagrams, nonequilibrium flux and nonequilibrium thermodynamic cost.

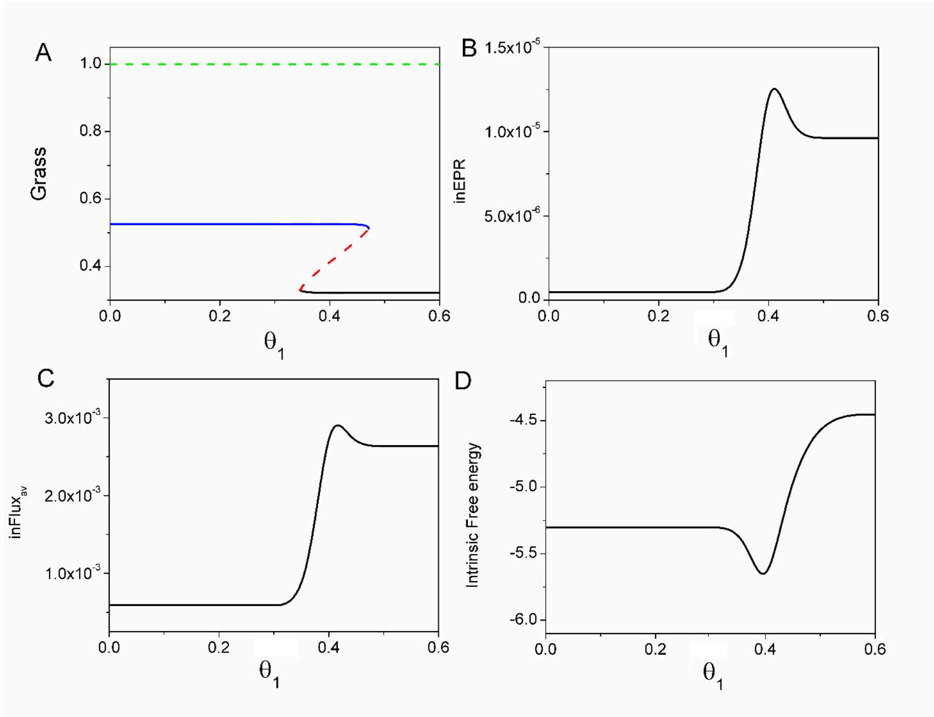

Fig. S18. A: The phase diagram versus θ_1. B: The intrinsic entropy production rate versus θ_1. C: The intrinsic average flux versus θ_1. D: Intrinsic free energy versus θ_1.

3.3.a. Finite fluctuations. Figure S13B shows the population entropy production rate versus θ_1, while Figure S13C shows the population average flux versus θ_1. Both population EPR and population $Flux_{av}$ increase as θ_1 increases. We can also see that both the two lines have a relative sharp changes in slopes in accordance with the bifurcation zone shown in Figure S13A. We found that the *Forest* state has more population EPR, population $Flux_{av}$ and the non-equilibrium intrinsic free energy than those of *Savanna* state.

3.3.b. The zero fluctuation limit. There are two phase transition points for this set of parameters shown in Figure S18A. Figure S18B shows the intrinsic entropy production rate versus θ_1. Figure S18C shows that the intrinsic average flux. The intrinsic intrinsic $Flux_{av}$ and intrinsic EPR are shown in Figure S18C.

4. Ecological behavior as a function of the savanna tree mortality rate ν.

4.1.Landscape, flux and dominant paths between different states.

4.1.a. Population-potential landscape and flux with finite fluctuation. Figure S19A shows the phase diagram, Figure S19B shows the population EPR, Figure S19C shows the average flux versus and Figure S20 shows the population-potential landscapes under finite fluctuations. Figure S21 shows the fluxes on the population-potential landscapes with respect to the increase of ν, which are shown as white arrows. Figure S21 also shows the dominant population paths on the population landscape U for different values of ν. The population action $A_{po}(\mathbf{x})$ is shown in Figure S22A and Figure S22D shows the logarithm of the dominant population path probability from the *Forest* state to the *Savanna* state divided by that of the dominant population path from the *Savanna* state to the *Forest* state.

4.1.b. Intrinsic potential landscape and flux velocity in the zero-fluctuation limit. Figure S23 shows the intrinsic potential landscape ϕ_0 for increasing ν, while Figure S24 shows the intrinsic potential landscape ϕ_0 in 2D under zero fluctuation limit. Figure S24 also shows the dominant intrinsic paths on the intrinsic potential landscape with the same coloring conventions as in the figures above. The intrinsic action $A_{in}(\mathbf{x})$ is shown in Figure S25A and Figure S25D shows the logarithm of the dominant intrinsic path probability from the *Forest* state to the *Savanna* state divided by that of the dominant intrinsic path from the *Savanna* state to the *Forest* state.

4.2.Barrier height and kinetic rates of switching. Figure S4D and Figure S5D show the barrier heights of the population-potential landscape the intrinsic barrier heights of the intrinsic potential landscape versus ν respectively. Figure S26 shows the logarithm of MFPT versus A:ν, B:ω_0, C:ω_1 and the logarithm of MFPT versus barrier heights for D: ν, E:ω_0, F: ω_1. We show the logarithm of MFPT versus ν in Figure S26A.

4.3. Bifurcation diagrams, nonequilibrium flux and nonequilibrium thermodynamic cost.

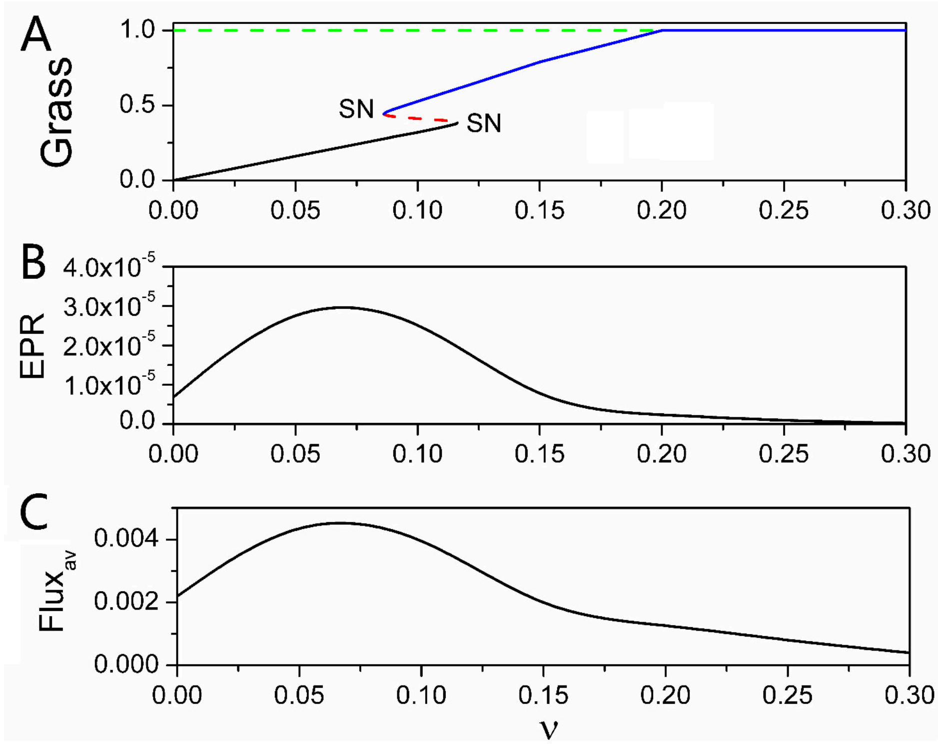

Fig. S19. A: The phase diagram versus ν. B: The population entropy production rate versus ν. C: The population average flux versus ν.

4.3.a. Finite fluctuations. Figure S19B shows the population EPR versus ν, while Figure S19C shows the average flux versus ν. The population EPR and population $Flux_{av}$ increase initially then decrease as ν increases. We can see that both the two lines have a relative significant changes in slopes in accordance with the bifurcation zone shown in Figure S19A. We found that the *Forest* state has more population EPR, population $Flux_{av}$ and the non-equilibrium intrinsic free energy than those of *Savanna*.

4.3.b. The zero fluctuation limit. There are two phase transition points for this set of parameters, as shown in Figure S27A. Figure S27B shows the intrinsic entropy production rate versus ν. Figure S27C shows the intrinsic average flux versus ν and Figure S27D shows the intrinsic free energy versus ν.

5. Ecological behavior as a function of the sapling-to-adult recruitment rate basic value ω_0.

5.1. Landscape, flux and dominant paths between different states.

5.1.a. Population-potential landscape and flux with finite fluctuations. Figure S28A shows the phase diagram versus ω_0. Figure S28B shows the population entropy production rate versus ω_0. Figure S28C shows the average flux versus ω_0 and Figure S29 shows the two-dimensional population-potential landscapes under finite fluctuations with respect to the increase of ω_0. Figure S30 shows the steady-state probability fluxes on the population-potential landscapes with respect to the increase of ω_0, which are shown as white arrows.

Figure S30 also shows the dominant population paths on the population landscape U for different values of ω_0. The population action $A_{po}(\mathbf{x})$ is shown in Figure S22B and Figure S22E shows the logarithm of the dominant population path probability from the *Forest* state to the *Savanna* state divided by that of the dominant population path from the *Savanna* state to the *Forest* state.

5.1.b. Non-equilibrium intrinsic potential landscape and the flux velocity in zero-fluctuation limit. Figure S31 shows the three-dimensional intrinsic potential landscape ϕ_0 for increasing ω_0. Figure S32 shows the two-dimensional non-equilibrium intrinsic potential landscape ϕ_0 under zero fluctuations and Figure S32 shows the dominant intrinsic paths on the intrinsic potential landscape ϕ_0 for different values of ω_0. The intrinsic action $A_{in}(\mathbf{x})$ is shown in Figure S25B and Figure S25E shows the logarithm of the dominant intrinsic path probability from the *Forest* state to the *Savanna* state divided by that of the dominant intrinsic path from the *Savanna* state to the *Forest* state.

5.2.Barrier height and kinetic rates of switching. Figure S4E and Figure S5E show the barrier heights of the population-potential landscape and the intrinsic barrier heights of the intrinsic potential landscape versus ω_0 respectively. We show the logarithm of MFPT versus ω_0 in Figure S26B. We can see the population-potential landscape topography quantified by the barrier height and the corresponding logarithm of MFPT have positive correlation shown in Figure S26E. Thus, the barrier height ΔU_F, ΔU_S and the corresponding MFPT $ln\tau_{FS}$, $ln\tau_{SF}$ have the correlation of $\tau \sim exp(\Delta U)$.

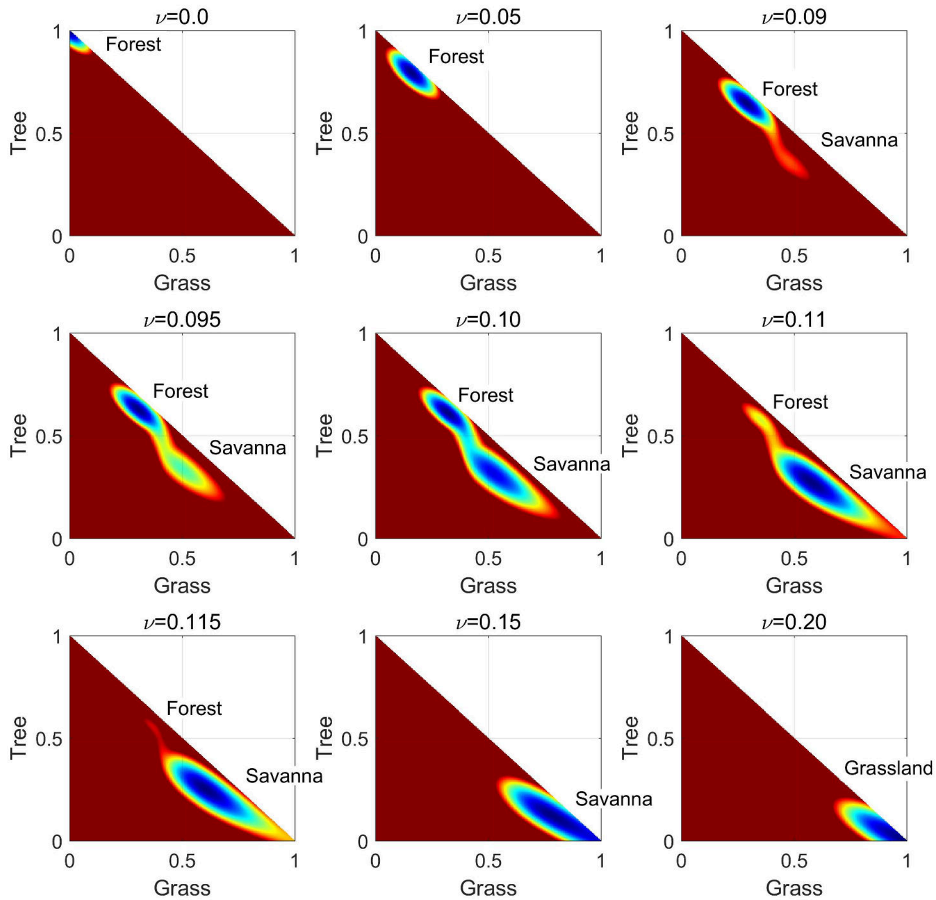

Fig. S20. The two-dimensional population-potential landscapes versus ν.

5.3. Bifurcation diagrams, nonequilibrium flux and nonequilibrium thermodynamic cost.

5.3.a. Finite fluctuations. Figure S28B shows the population entropy production rate versus ω_0. Figure S28C shows the average flux versus ω_0. We can see both population EPR and population $Flux_{av}$ increase as ω_0 increases. We can see both the two lines have a relative significant changes in slopes near (between) the two saddle-node bifurcations shown in Figure S28A. The *Forest* state has more population EPR, population $Flux_{av}$ and the non-equilibrium intrinsic free energy than those of *Savanna* state.

5.3.b. The zero fluctuation limit. There are two phase transition points for this set of parameters which is shown in Figure S33A. Figure S33B shows the intrinsic entropy production rate versus ω_0 and Figure S33C shows the intrinsic average flux versus ω_0.

6. Ecological behavior as a function of the savanna sapling-to-adult recruitment rate of sigmoid basic value ω_1.

6.1.Landscape, flux and dominant paths between different states.

6.1.a. Population-potential landscape and flux with finite fluctuations. ω_1 is the savanna sapling-to-adult recruitment rate minimum in the function ω. Figure S34A shows the phase diagram, Figure S34B shows the population entropy production rate, and Figure S34C shows the average flux versus ω_1. Figure S35 and Figure S36 show the two-dimensional population-potential landscapes under finite fluctuations and the fluxes on the population landscapes respectively.

6.1.b. Intrinsic potential landscape and flux velocity in the zero-fluctuation limit. Figure S37 shows the three-dimensional intrinsic potential landscape ϕ_0 with increasing ω_1, while Figure S38 shows the two-dimensional non-equilibrium intrinsic potential landscape ϕ_0 for increasing ω_1 along with the dominant intrinsic paths. The intrinsic action $A_{in}(\mathbf{x})$ is shown in Figure S25C and Figure S25F shows the logarithm of the dominant intrinsic path probability from the *Forest* state to the *Savanna* state divided by that of the dominant intrinsic path from the *Savanna* state to the *Forest* state.

6.2.Barrier height and kinetic rates of switching. Figure S4F and Figure S5F show the barrier heights of the population-potential landscape under finite fluctuations and the intrinsic barrier heights of the intrinsic potential landscape versus ω_1 respectively. s_1 is the saddle point between *Forest* state and *Savanna* state. s_2 is the saddle point between *Grassland* state and *Savanna* state. s_3 is the saddle point between *Grassland* state and *Forest* state with small ω_1. Thus, $\Delta U_F = U_{s1} - U_F$ or $\Delta U_F = U_{s3} - U_F$,

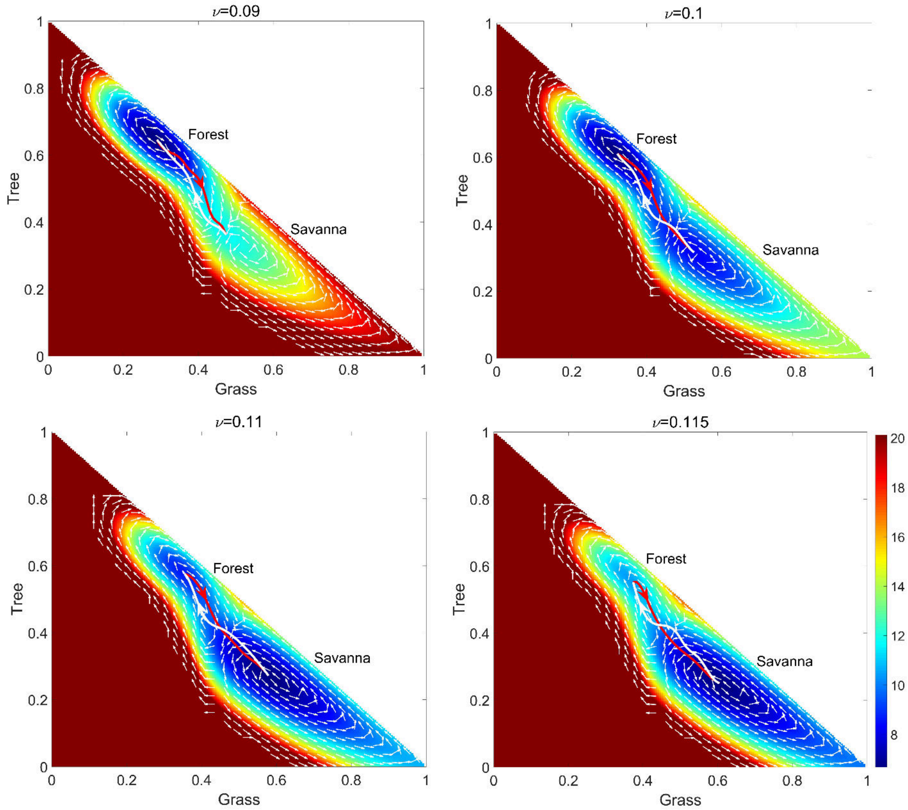

Fig. S21. The dominant population paths and fluxes on the population-potential landscape U with different ν, at $\beta = 0.38, \theta_1 = 0.4, \omega_0 = 0.9, \omega_1 = 0.2, \mu = 0.2, s_1 = 0.01$, $D = 0.0005$. The white lines represent the dominant population paths from the $Savanna$ state to $Forest$ state. The red lines represent the dominant population paths from the $Forest$ state to $Savanna$ state. The white arrows represent the steady-state probability fluxes.

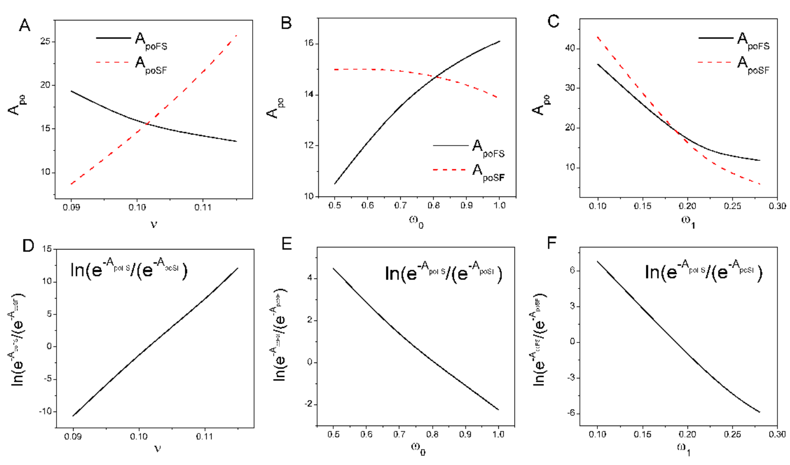

Fig. S22. A: The population action A_{poFS} of the probability of the dominant population path from $Forest$ state to $Savanna$ state and the action A_{poSF} of the probability of the dominant population path from $Savanna$ state to $Forest$ state versus ν. D:The probability of the dominant population path from $Forest$ state to $Savanna$ state divided that of the dominant population path from $Savanna$ state to $Forest$ state versus ν with $\beta = 0.38, \omega_0 = 0.9, \omega_1 = 0.2, \theta_1 = 0.4, ss_1 = 0.01, \mu = 0.2$. B: The population action A_{poFS} and A_{poSF} versus ω_0. E:The probability of the dominant population path from $Forest$ state to $Savanna$ state divided that of the dominant population path from $Savanna$ state to $Forest$ state versus ω_0 with $\beta = 0.38, \nu = 0.1, \mu = 0.2, \omega_1 = 0.2, \theta_1 = 0.4, ss_1 = 0.01$. C: The population action A_{poFS} and A_{poSF} versus ω_1. F:The probability of the dominant population path from $Forest$ state to $Savanna$ state divided that of the dominant population path from $Savanna$ state to $Forest$ state versus ω_1 with $\beta = 0.38, \nu = 0.1, \omega_0 = 0.9, \theta_1 = 0.4, ss_1 = 0.01, \mu = 0.2$.

$\Delta U_S = U_{s1} - U_S$, $\Delta U_{Ss_2} = U_{s2} - U_S$, $\Delta U_G = U_{s2} - U_G$ and $\Delta U_{Gs_3} = U_{s3} - U_G$. We show the logarithm of MFPT versus ω_1 in Figure S26C. We can see that the population-potential landscape topography quantified by the barrier height and the

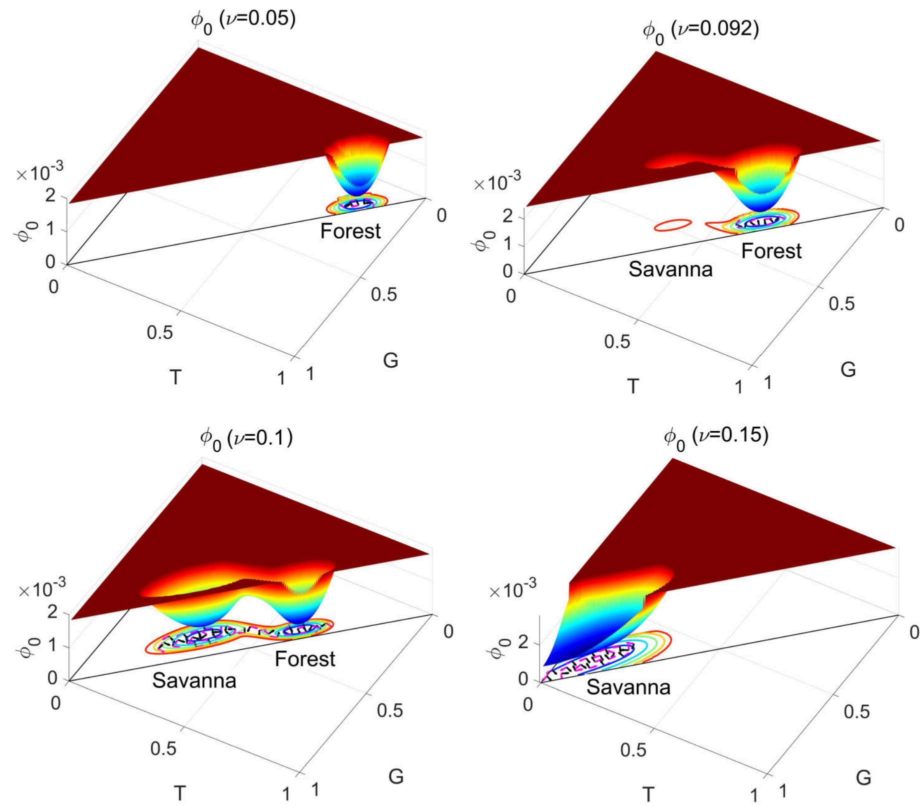

Fig. S23. The three-dimensional intrinsic potential landscape ϕ_0 for increasing ν. The projection of the flux velocity (purple arrows)and the gradient of the intrinsic potential landscape $-\nabla\phi_0$ (black arrows)on the intrinsic potential landscape ϕ_0 for increasing ν.

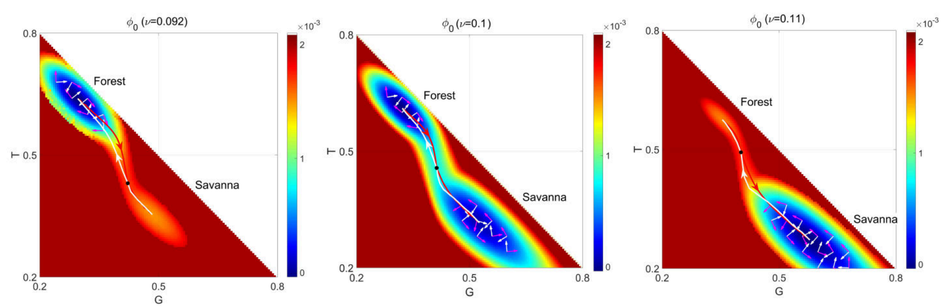

Fig. S24. The projection of the flux velocity (purple arrows)and the gradient of the intrinsic potential landscape $-\nabla\phi_0$ (white arrows)on the intrinsic potential landscape ϕ_0 for increasing ν. The dominant intrinsic paths on the intrinsic potential landscape ϕ_0 with different ν. The white lines represent the dominant intrinsic paths from the $Savanna$ state to $Forest$ state. The red lines represent the dominant intrinsic paths from the $Forest$ state to $Savanna$ state.

corresponding logarithm of MFPT have positive correlation shown in Figure S26F. Thus, the barrier height ΔU_F, ΔU_S and the corresponding MFPT $ln\tau_{FS}$, $ln\tau_{SF}$ have the correlation of $\tau \sim exp(\Delta U)$.

6.3. Bifurcation diagrams, nonequilibrium flux and nonequilibrium thermodynamic cost.

6.3.a. Finite fluctuations. Figure S34B and S34C show the population EPR and the population average flux versus ω_1, while the corresponding bifurcations diagram is shown in Figure S34A.

6.3.b. The zero fluctuation limit. There are two phase transition points for this set of parameters, as shown in Figure S39A. Figure S39B and S39C show the intrinsic EPR and the intrinsic average flux versus ω_1. Figure S39D shows the intrinsic free energy versus ω_1.

6.4. The average change of the forward and backward in time cross-correlation function, the variances grass and trees, and the logarithms of the variances of the first passage time. Figure S40 shows the average change of the forward and backward in time cross correlation function ΔCC as a function of different parameter A:μ, B: θ_1, C:ν, D:ω_0, E:ω_1. Figure S41 shows the variances $Grass$ σ_S and

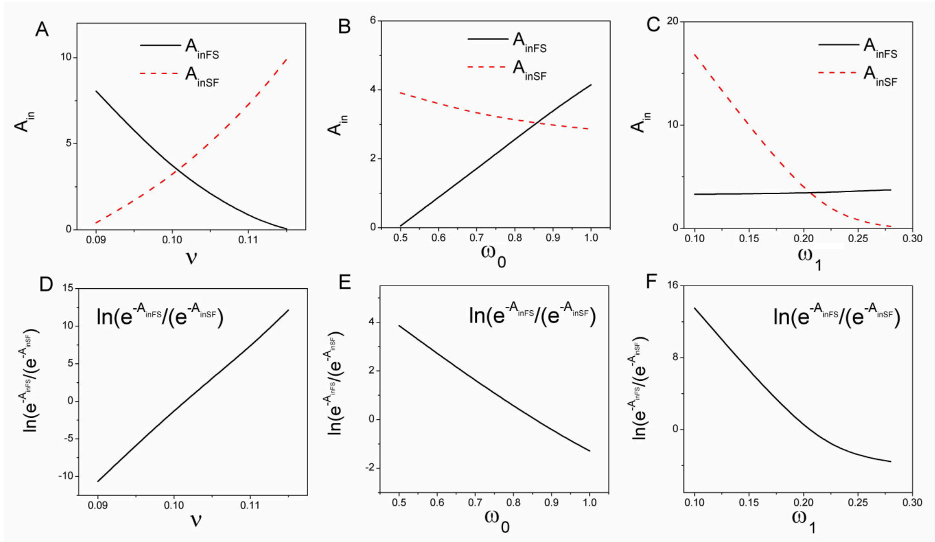

Fig. S25. A: The intrinsic action A_{inFS} of the probability of the dominant intrinsic path from $Forest$ state to $Savanna$ state and the intrinsic action A_{inSF} of the probability of the dominant intrinsic path from $Savanna$ state to $Forest$ state versus ν. D:The probability of the dominant intrinsic path from $Forest$ state to $Savanna$ state divided that of the dominant intrinsic path from $Savanna$ state to $Forest$ state versus ν with $\beta = 0.38, \omega_0 = 0.9, \omega_1 = 0.2, \theta_1 = 0.4, ss_1 = 0.01, \mu = 0.2$. B: The intrinsic action A_{inFS} and A_{inSF} versus ω_0. E:The probability of the intrinsic dominant intrinsic path from $Forest$ state to $Savanna$ state divided that of the dominant intrinsic path from $Savanna$ state to $Forest$ state versus ω_0 with $\beta = 0.38, \nu = 0.1, \mu = 0.2, \omega_1 = 0.2, \theta_1 = 0.4, ss_1 = 0.01$. C: The intrinsic action A_{inFS} and A_{inSF} versus ω_1. F:The probability of the dominant intrinsic path from $Forest$ state to $Savanna$ state divided that of the dominant intrinsic path from $Savanna$ state to $Forest$ state versus ω_1 with $\beta = 0.38, \nu = 0.1, \omega_0 = 0.9, \theta_1 = 0.4, ss_1 = 0.01, \mu = 0.2$.

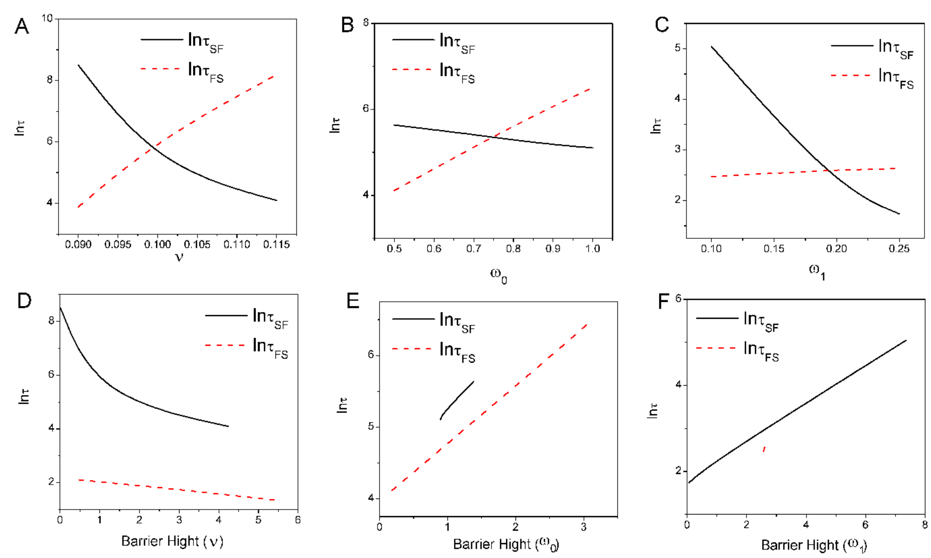

Fig. S26. The logarithm of MFPT versus A:ν, B:ω_0, C:ω_1. The logarithm of MFPT versus barrier heights for D: ν, E:ω_0, F: ω_1.

the variances *Tree* σ_F versus A:μ, B: θ_1, C:ν, D:ω_0, E:ω_1. Figure S42 shows the logarithms of the variances of the first passage time from *Savanna* to *Forest* $\log(\sigma_{SF})$ and the first passage time from *Forest* to *Savanna* $\log(\sigma_{FS})$, and the logarithms of the sum of them $\log(\sigma_{SF} + \sigma_{FS})$ with A:μ, B: θ_1, C:ν, D:ω_0, E:ω_1.

7. The intrinsic potential landscape ϕ_0 and the Hamilton-Jacobi equation for a specific diffusion matrix. We obtain the intrinsic potential landscape ϕ_0 by the fitting method described in the main text due to the constraint of a triangle state space. In order to find the intrinsic Lyapunov function $\phi_0(\mathbf{D})$ numerically, we choose the diffusion matrix $\mathbf{D} = D\mathbf{G}$ with the form $G_{ij} = x_i(\delta_{ij} - x_j)$. This diffusion coefficient matrix originates from evolutionary population dynamics (5, 6). The diffusion coefficient matrix is thus given by:

$$\mathbf{G} = \begin{pmatrix} x_1(1-x_1) & -x_1x_2 & -x_1x_3 \\ -x_2x_1 & x_2(1-x_2) & -x_2x_3 \\ -x_3x_1 & -x_3x_2 & x_3(1-x_3) \end{pmatrix} \qquad [1]$$

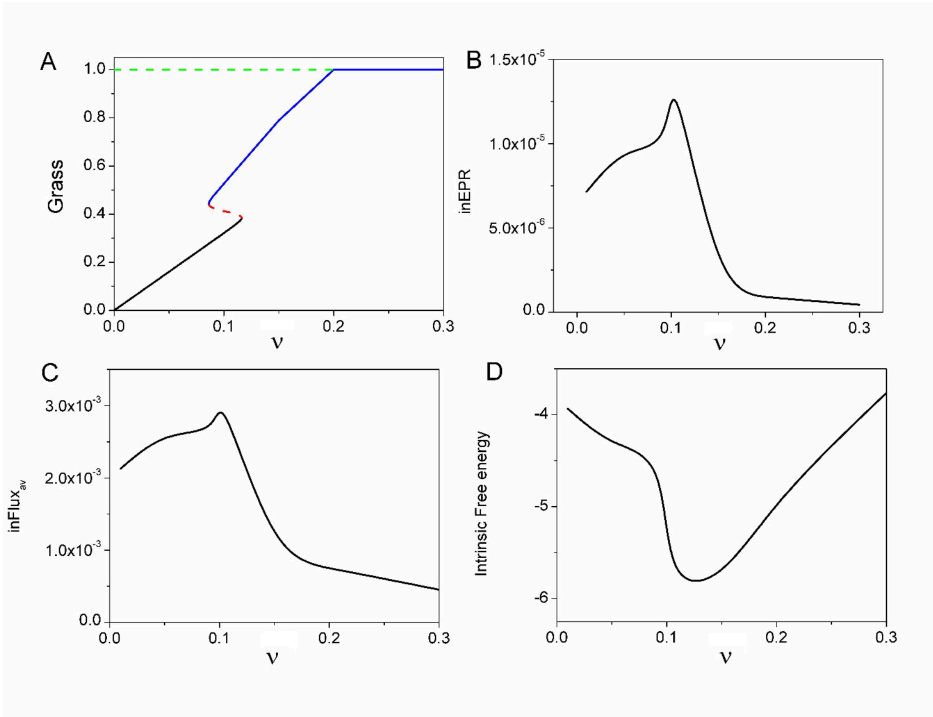

Fig. S27. A: The phase diagram versus ν. B: The intrinsic entropy production rate versus ν. C: The intrinsic average flux versus ν. D: Intrinsic free energy versus ν.

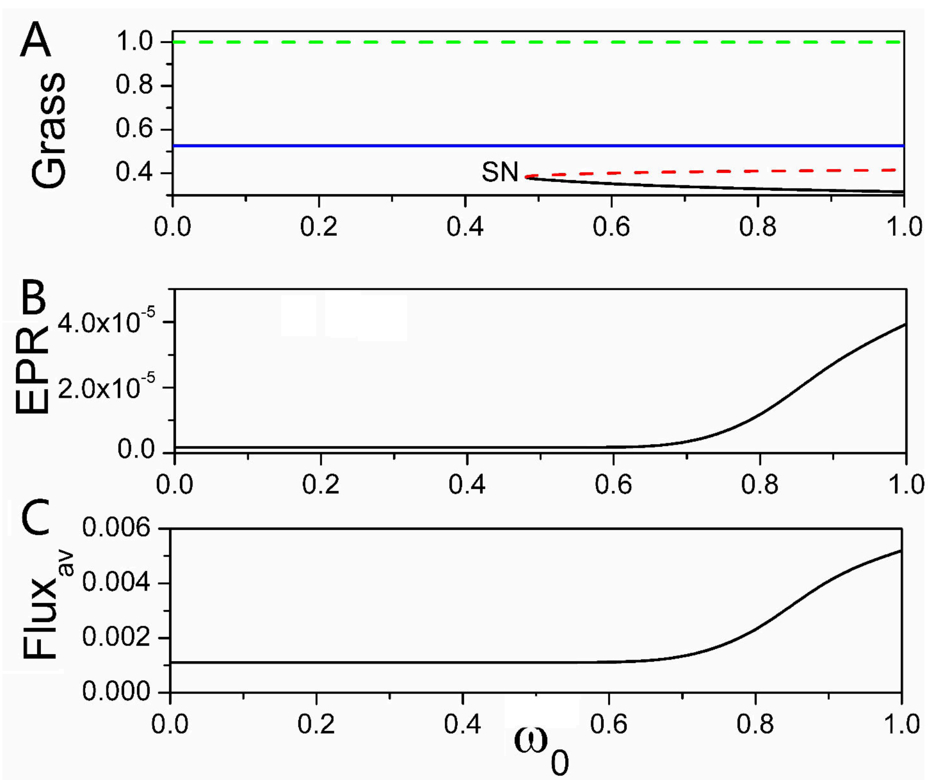

Fig. S28. A: The phase diagram versus ω_0. B: The population entropy production rate versus ω_0. C: The population average flux versus ω_0.

Since the three variables satisfy the normalization condition $G + S + T = 1$ ($x_1 + x_2 + x_3 = 1$), the dimensionality of the forest-savanna ecological system will reduce from a three-dimensional system with the fraction of grass coverage ($G = x_1$), savanna saplings ($S = x_3$) and trees ($T = x_2$) to a an effective two-dimensional system. The corresponding state space has the shape of an isosceles triangle. Unfortunately, it is very difficult to solve a Hamilton-Jacobi equation in a isosceles triangle

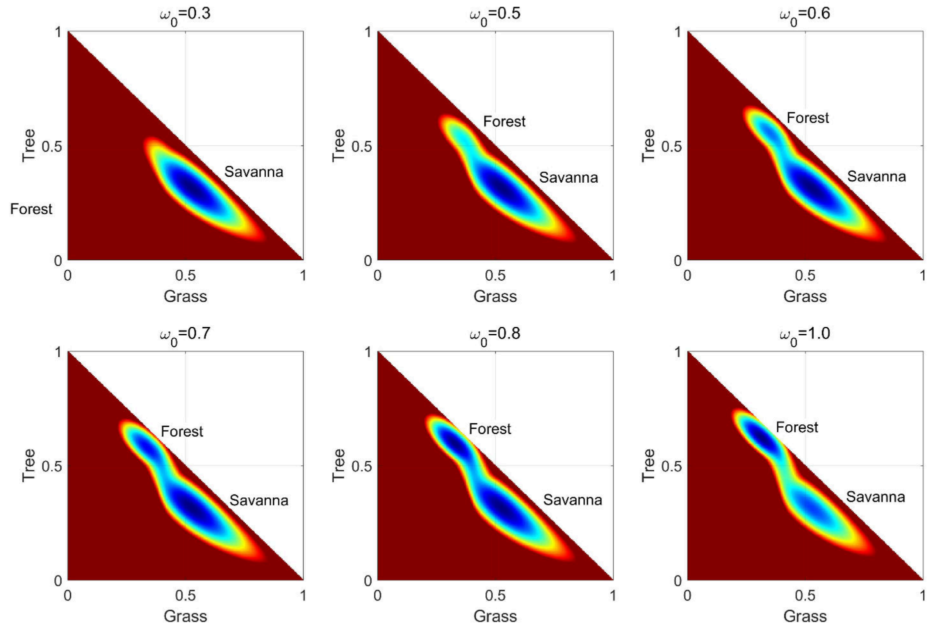

Fig. S29. The two-dimensional population-potential landscapes versus ω_0.

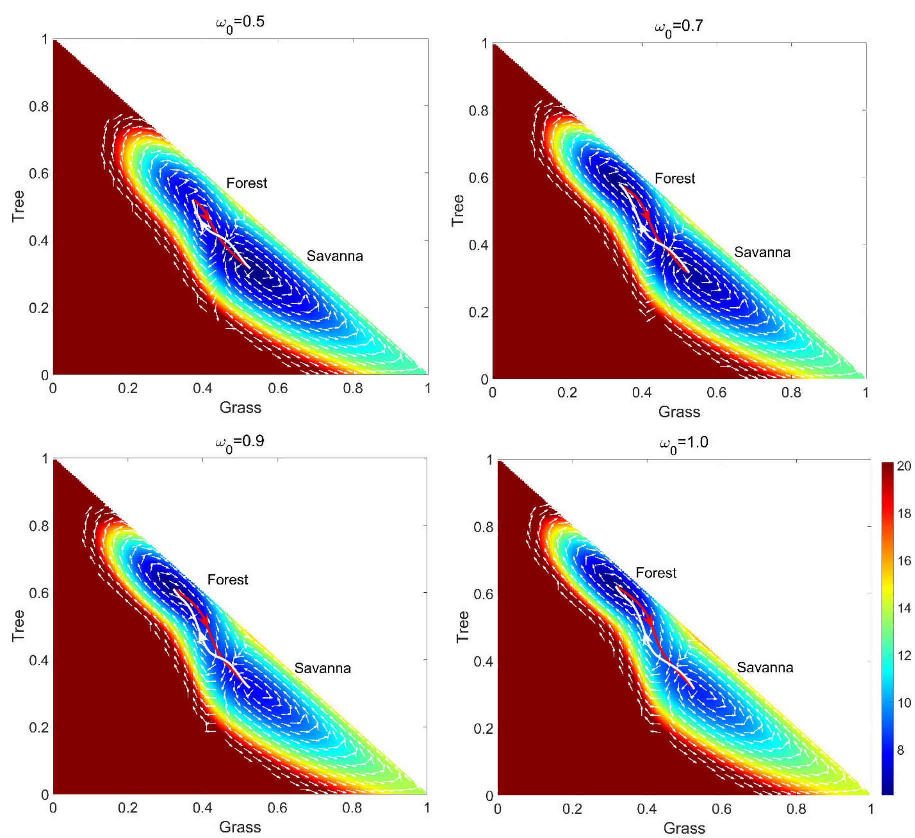

Fig. S30. The dominant population paths and fluxes on the population-potential landscape U with different ω_0, at $\beta = 0.38, \theta_1 = 0.4, \nu = 0.1, \omega_1 = 0.2, \mu = 0.2, s_1 = 0.01$, $D = 0.0005$. The white lines represent the dominant population paths from the $Savanna$ state to $Forest$ state. The red lines represent the dominant population paths from the $Forest$ state to $Savanna$ state. The white arrows represent the steady-state probability fluxes.

and we can only numerical solve Hamilton-Jacobi equation in regular shapes, such as squares and rectangles with a diagonal diffusion matrix (6–8). Our particular choice of diffusion coefficient matrix enables us to perform the coordinate transformation from a special diffusion matrix in an isosceles triangle into a diagonal matrix in a square (8).

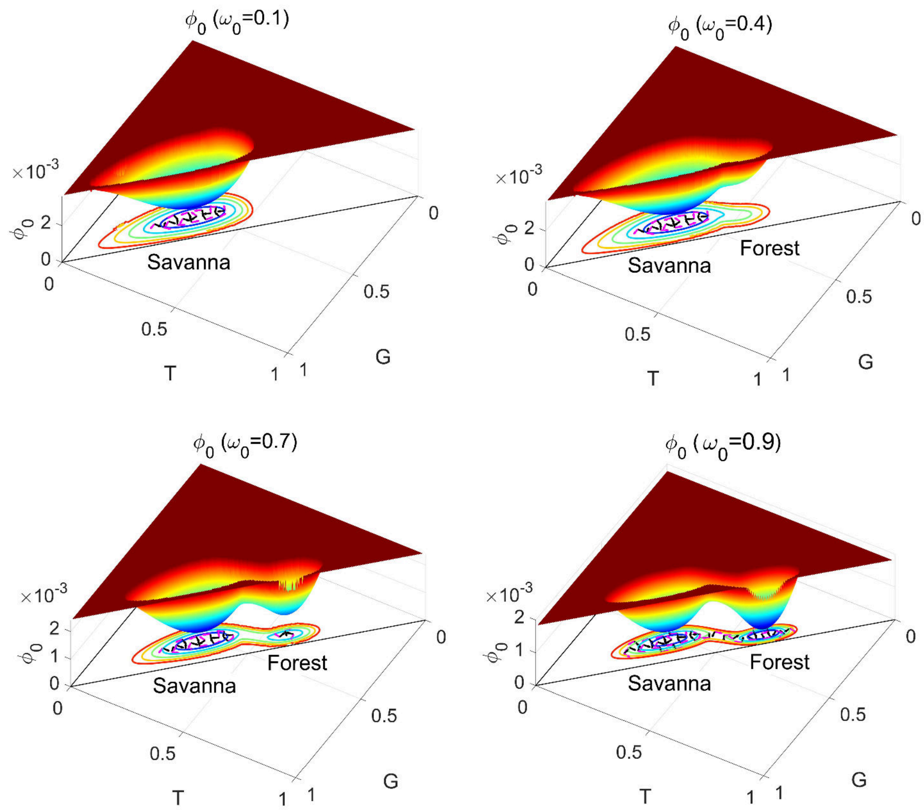

Fig. S31. The three-dimensional intrinsic potential landscape ϕ_0 for increasing ω_0. The projection of the flux velocity (purple arrows)and the gradient of the intrinsic potential landscape $-\nabla\phi_0$ (black arrows)on the intrinsic potential landscape ϕ_0 for increasing ω_0.

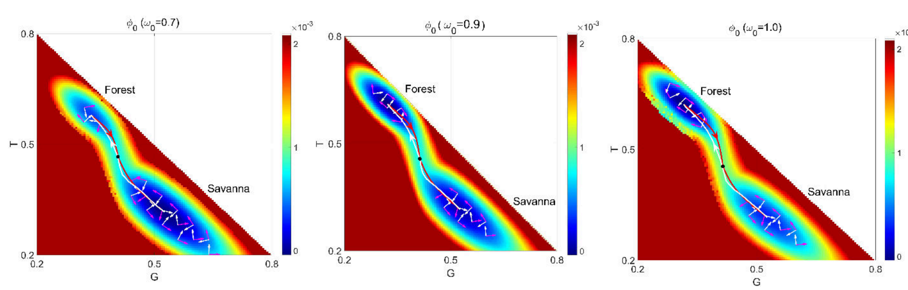

Fig. S32. The projection of the flux velocity (purple arrows)and the gradient of the intrinsic potential landscape $-\nabla\phi_0$ (white arrows)on the intrinsic potential landscape ϕ_0 for increasing ω_0. The dominant intrinsic paths on the intrinsic potential landscape ϕ_0 with different ω_0. The white lines represent the dominant intrinsic paths from the $Savanna$ state to $Forest$ state. The red lines represent the dominant intrinsic paths from the $Forest$ state to $Savanna$ state.

The transformation of the original coordinate system in term of the probability of G, S, T is to obtain a Hamilton-Jacobi equation with diagonal matrix. We set $u_1 = x_1, u_2 = x_2/(1-x_1)$. Therefore, new coordinate variables are satisfied with $0 \leq u_1, u_2 \leq 1$. We show the original coordinate in Figure S43A while the new coordinate in Figure S43B. The different colored lines in Figure S43A transform to the lines in Figure S43B (8). The grid points in Figure S43A transform to as the dot lines in Figure S43B. Thus, the inverse transformation is $x_1 = u_1, x_2 = u_2(1-u_1)$. And the nondiagonal elements of the new diffusion matrix are equal to zero ($D^u_{ij} = 0, i \neq j$). This transformation of the variables can lead to a new Hamilton-Jacobi equation with the same form as the original one, but in diagonal form. Due to the form of the diffusion matrix, there are no mixed second-order derivatives(8). Thus, the Hamilton-Jacobi equation with the given diffusion matrix in the isosceles triangle is transformed to the diagonal diffusion matrix in a square and we can solve for the intrinsic potential via the new Hamilton-Jacobi equation. Using the inverse transformation, we can obtain the intrinsic potential of the original Hamilton-Jacobi equation (8). We use a numerical level set method with the Mitchell's level-set toolbox to solve the Hamilton-Jacobi equation for intrinsic potential ϕ_0(9).

Figure S44 shows the dominant intrinsic paths on the intrinsic landscape ϕ_0 with different β. The red lines are the dominant intrinsic paths from the *Forest* state to *Savanna* state and the white lines are the dominant intrinsic paths from the *Savanna* state to *Forest* state.

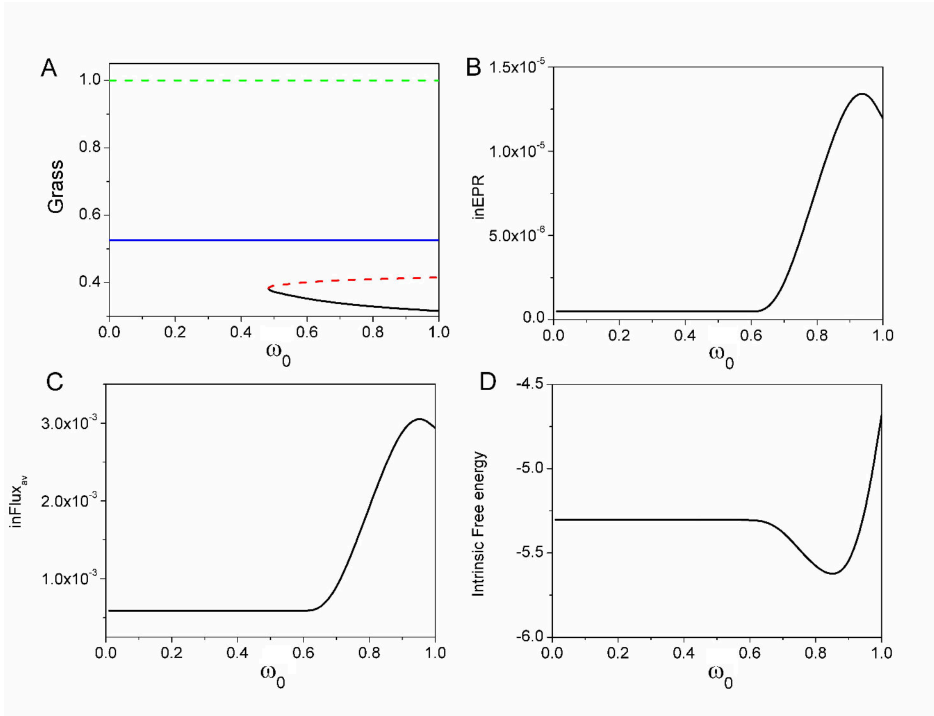

Fig. S33. A: The phase diagram versus ω_0. B: The intrinsic entropy production rate versus ω_0. C: The intrinsic average flux versus ω_0. D: Intrinsic free energy versus ω_0.

References

1. NG Van Kampen, Stochastic processes in physics and chemistry. (Elsevier) Vol. 1, (1992).
2. A Terebus, C Liu, J Liang, Discrete and continuous models of probability flux of switching dynamics: Uncovering stochastic oscillations in a toggle-switch system. The Journal of Chemical Physics **151**, 185104 (2019).
3. A Terebus, C Liu, J Liang, Discrete flux and velocity fields of probability and their global maps in reaction systems. The Journal of Chemical Physics **149**, 185101 (2018).
4. Y Xu, R Gu, H Zhang, W Xu, J Duan, Stochastic bifurcations in a bistable Duffing–Van der Pol oscillator with colored noise. Physical Review E **83**, 056215 (2011).
5. SH Rice, Evolutionary theory: mathematical and conceptual foundations. (Sinauer Associates), (2004).
6. F Zhang, L Xu, K Zhang, E Wang, J Wang, The potential and flux landscape theory of evolution. The Journal of chemical physics **137**, 065102 (2012).
7. L Xu, F Zhang, K Zhang, E Wang, J Wang, The potential and flux landscape theory of ecology. PLoS One **9**, e86746 (2014).
8. GJ Baxter, RA Blythe, AJ McKane, Exact solution of the multi-allelic diffusion model. Mathematical biosciences **209**, 124–170 (2007).
9. IM Mitchell, The flexible, extensible and efficient toolbox of level set methods. Journal of Scientific Computing **35**, 300–329 (2008).

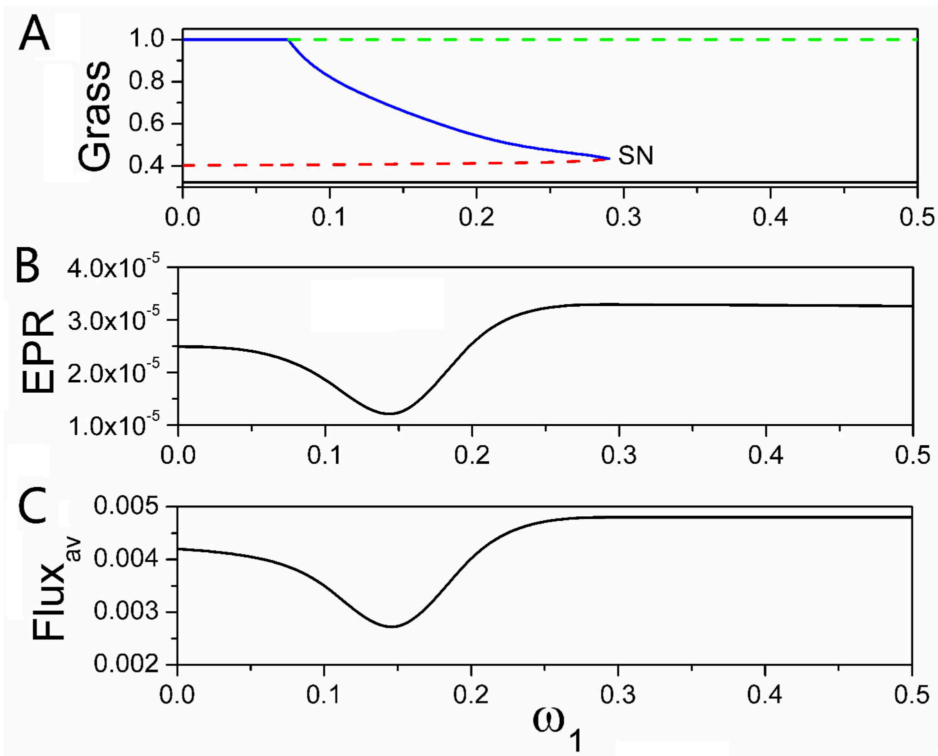

Fig. S34. A: The phase diagram versus ω_1. B: The population entropy production rate versus ω_1. C: The population average flux versus ω_1.

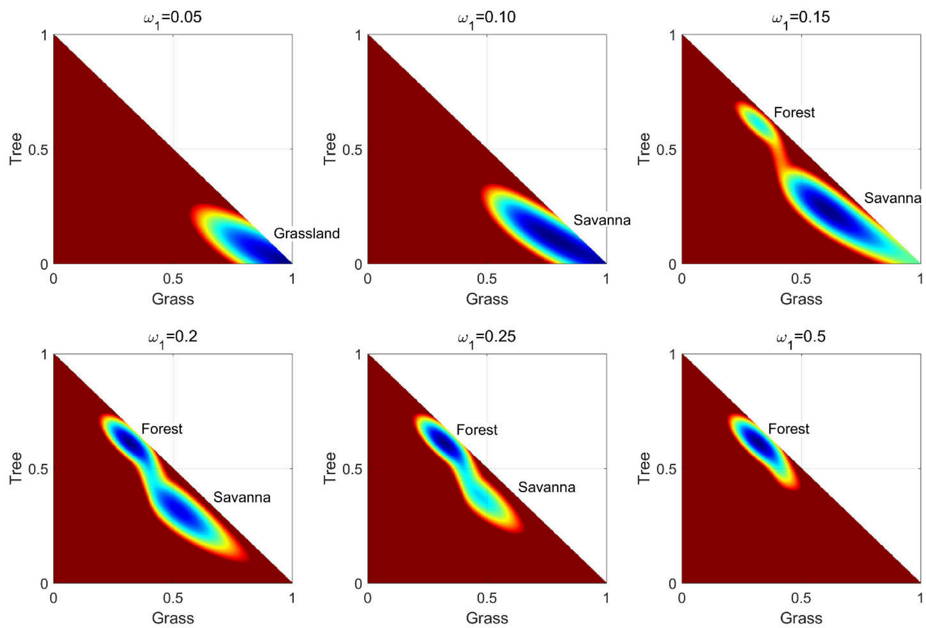

Fig. S35. The two-dimensional population-potential landscapes versus ω_1.

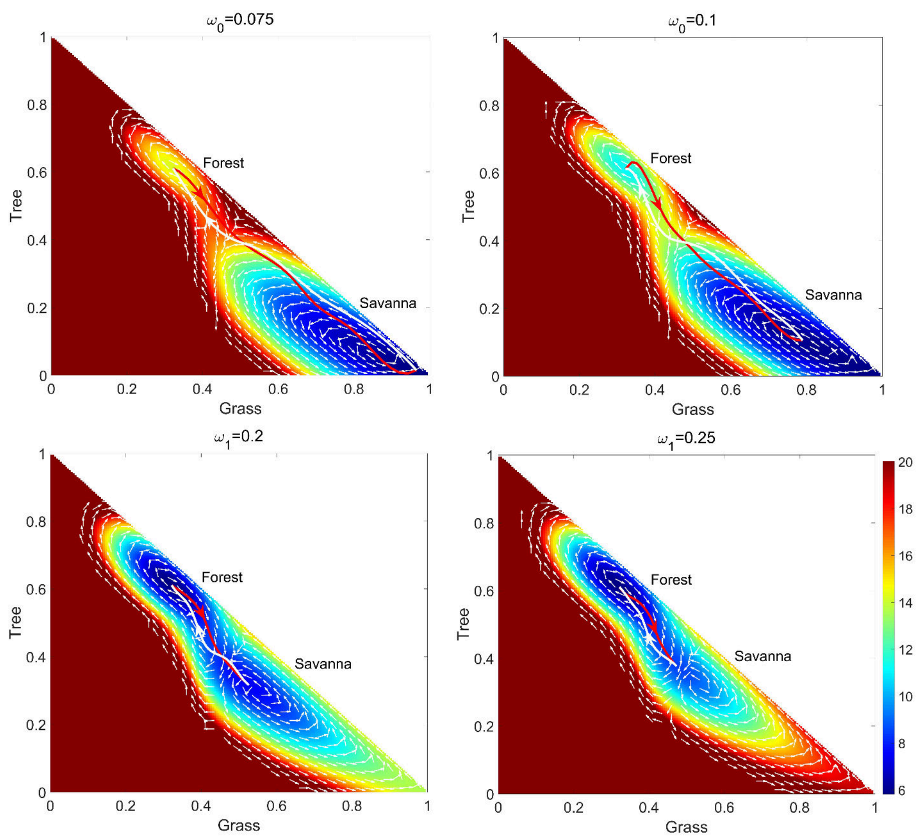

Fig. S36. The dominant population paths and fluxes on the population-potential landscape U with different ω_1, at $\beta = 0.38, \theta_1 = 0.4, \nu = 0.1, \omega_0 = 0.9, \mu = 0.2, s_1 = 0.01, D = 0.0005$. The white lines represent the dominant population paths from the $Savanna$ state to $Forest$ state. The red lines represent the dominant population paths from the $Forest$ state to $Savanna$ state. The white arrows are the steady-state probability fluxes.

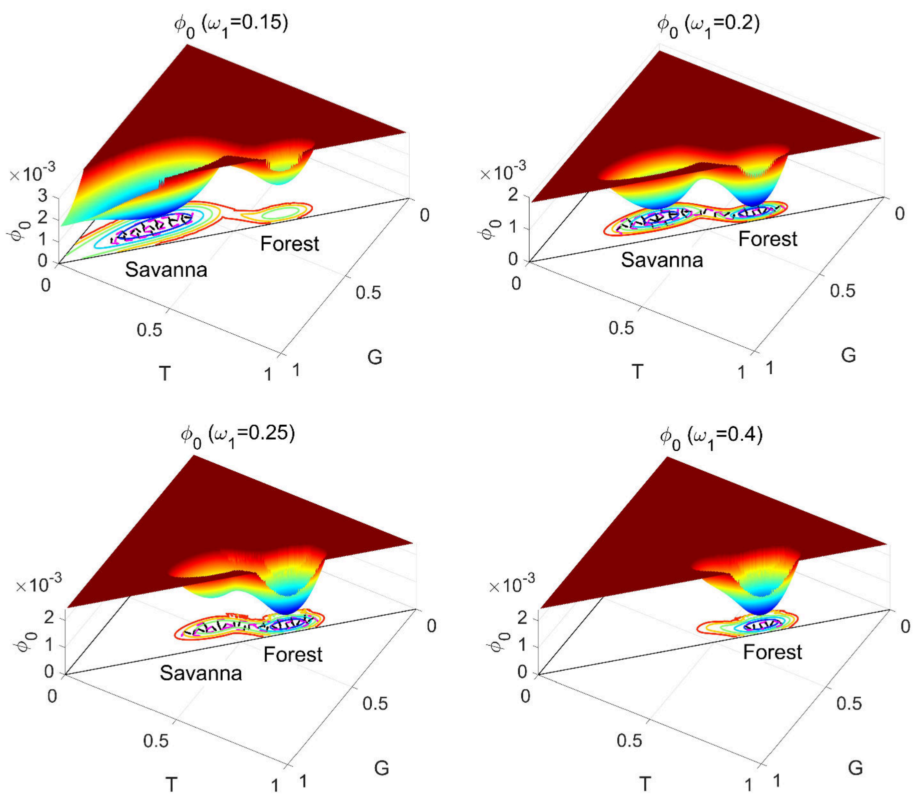

Fig. S37. The three-dimensional intrinsic potential landscape ϕ_0 for increasing ω_1. The projection of the flux velocity (purple arrows)and the gradient of the intrinsic potential landscape $-\nabla\phi_0$ (black arrows)on the intrinsic potential landscape ϕ_0.

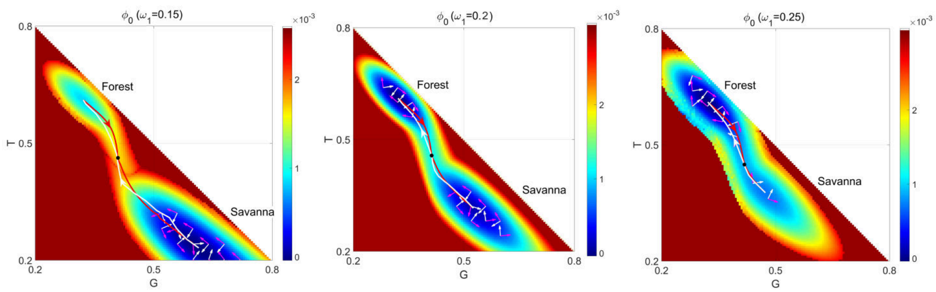

Fig. S38. The projection of the flux velocity (purple arrows)and the gradient of the intrinsic potential landscape $-\nabla\phi_0$ (white arrows)on the intrinsic potential landscape ϕ_0 for increasing ω_1. The dominant intrinsic paths on the intrinsic potential landscape ϕ_0 with different ω_1. The white lines represent the dominant intrinsic paths from the $Savanna$ state to $Forest$ state. The red lines represent the dominant intrinsic paths from the $Forest$ state to $Savanna$ state.

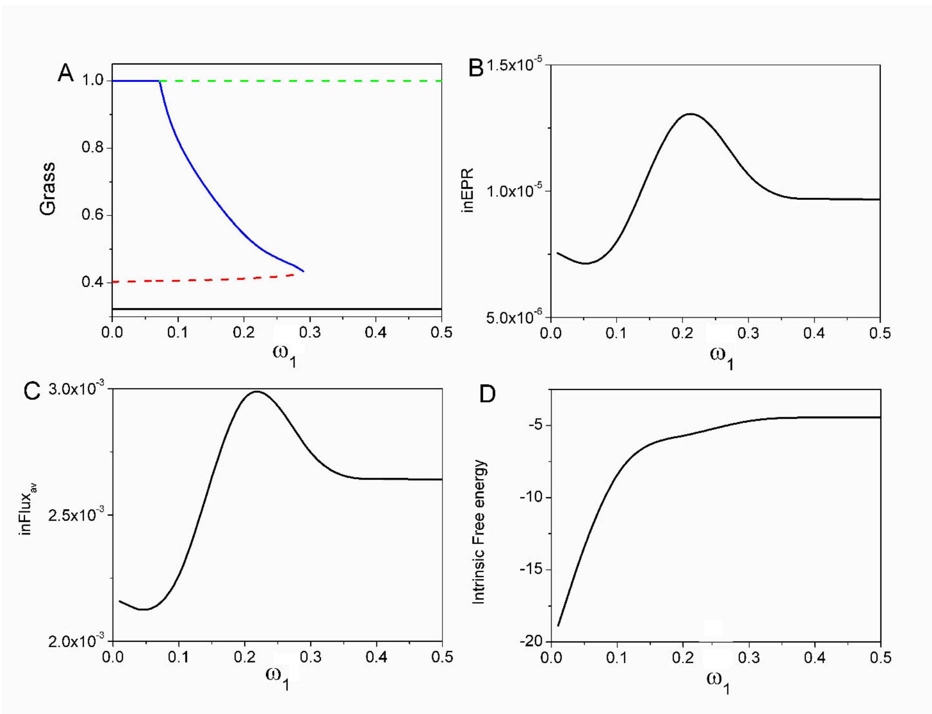

Fig. S39. A: The phase diagram versus ω_1. B: The intrinsic entropy production rate versus ω_1. C: The intrinsic average flux versus ω_1. D: Intrinsic free energy versus ω_1.

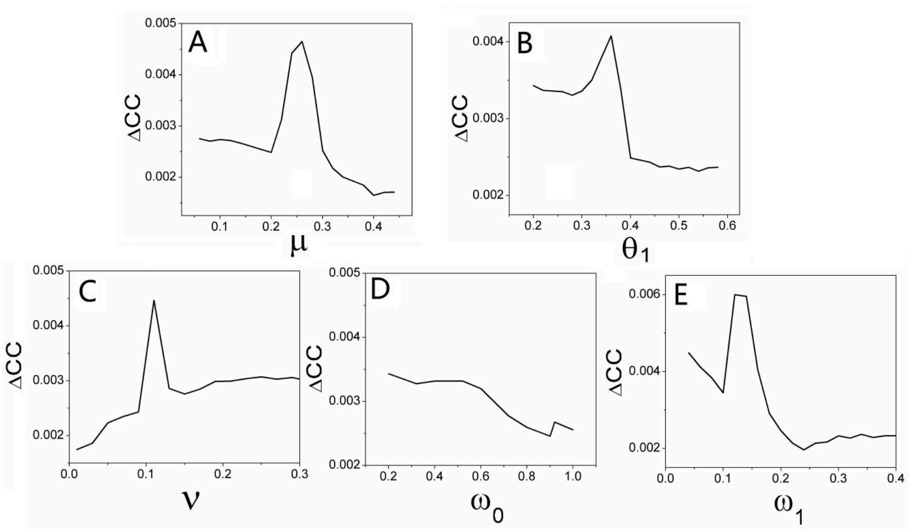

Fig. S40. The average change of the forward and backward in time cross correlation function ΔCC as a function of different parameters. A:μ, B: θ_1, C:ν, D:ω_0, E:ω_1.

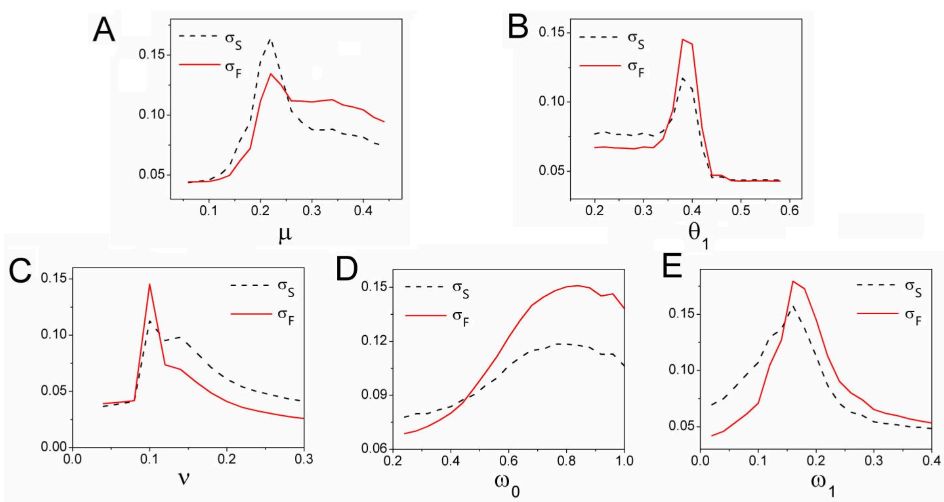

Fig. S41. The variances $Grass\ \sigma_S$ and the variances $Tree\ \sigma_F$ versus A:μ, B: θ_1, C:ν, D:ω_0, E:ω_1.

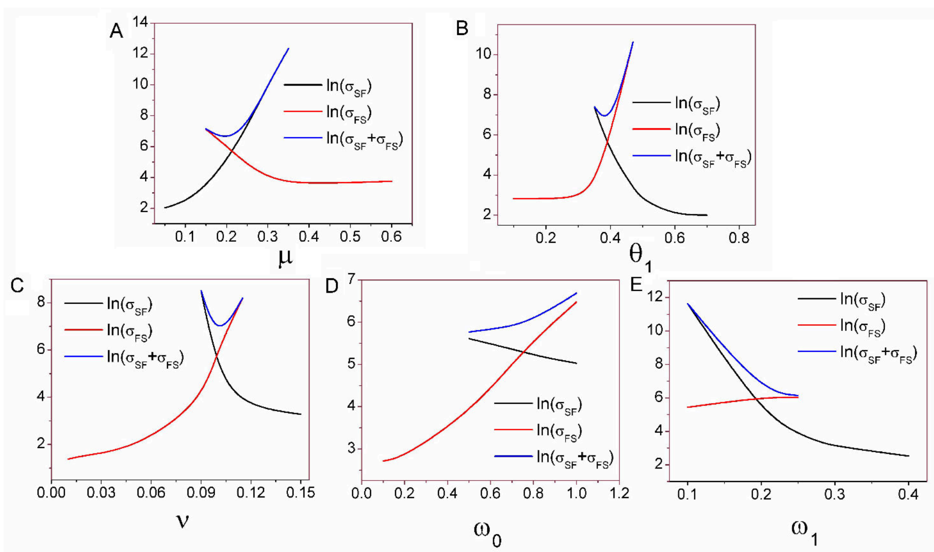

Fig. S42. The logarithms of the variances of the first passage time from $Savanna$ to $Forest$ $\log(\sigma_{SF})$ and the first passage time from $Forest$ to $Savanna$ $\log(\sigma_{FS})$, and the logarithms of the sum of them $\log(\sigma_{SF} + \sigma_{FS})$ with A:μ, B: θ_1, C:ν, D:ω_0, E:ω_1.

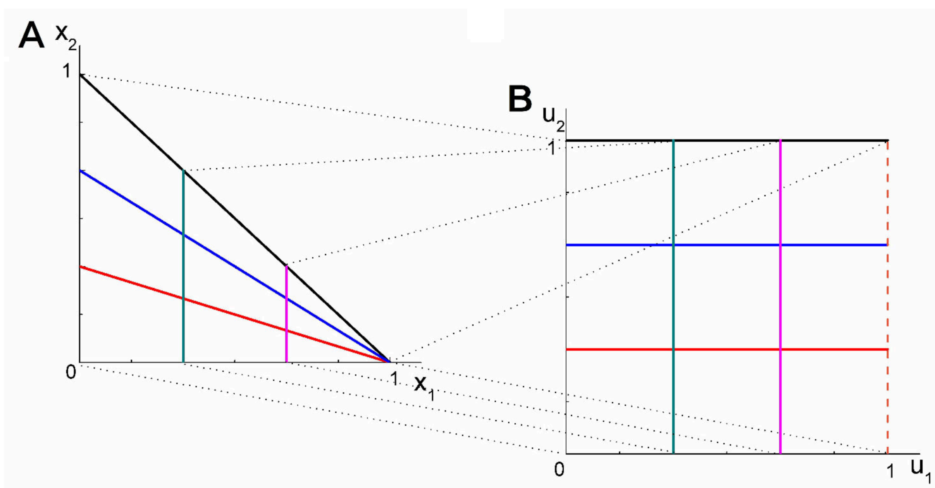

Fig. S43. Schematic representation of the transformation of the coordinates from $x_1 - x_2$ plane to $u_1 - u_2$ plane(8).

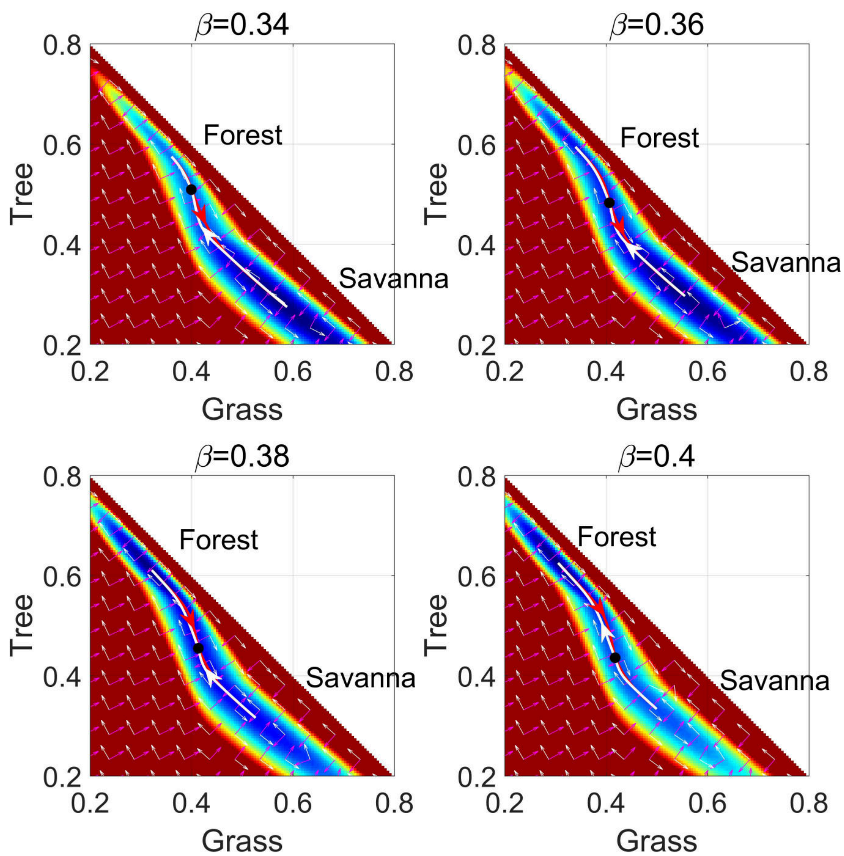

Fig. S44. The dominant intrinsic paths on the intrinsic potential landscape ϕ_0 with different β from Hamilton-Jacobi equation with a chosen diffusion matrix. The white lines represent the dominant intrinsic paths from the $Savanna$ state to $Forest$ state. The red lines represent the dominant intrinsic paths from the $Forest$ state to $Savanna$ state. White arrows represents the projection of the flux velocity and purple arrows represents the negative gradient of the intrinsic landscape $-\nabla\phi_0$.